UNIVERSITY OF WARMIA AND MAZURY IN OLSZTYN

Technical Sciences

22(3) 2019

OLSZTYN 2019

The Technical Sciences is indexed and abstracted in BazTech (http://baztech.icm.edu.pl) and in IC Journal Master List (http://journals.indexcopernicus.com)

The Journal is available in electronic form on the web sites
http://www.uwm.edu.pl/techsci (subpage Issues)
http://wydawnictwo.uwm.edu.pl (subpage Czytelnia)

The electronic edition is the primary version of the Journal

PL ISSN 1505-4675
e-ISSN 2083-4527

Address
ul. Jana Heweliusza 14
10-718 Olsztyn-Kortowo, Poland
tel.: +48 89 523 36 61
fax: +48 89 523 34 38
e-mail: wydawca@uwm.edu.pl

Ark. wyd. 6,5, ark. druk. 5,5, nakład 75 egz.
Druk – Zakład Poligraficzny UWM, zam. 112

Contents

Technical Sciences, 2019, 22(3), 205–220

UNIWERSYTET WARMIŃSKO-MAZURSKI W OLSZTYNIE

Quarterly peer-reviewed scientific journal
ISSN 1505-4675
e-ISSN 2083-4527
TECHNICAL SCIENCES
Homepage: www.uwm.edu.pl/techsci/

doi: 10.31648/ts.4352

FLUID FLOW IN THE IMPULSE VALVE OF A HYDRAULIC RAM

Wojciech Sobieski[1], *Dariusz Grygo*[2]

[1]ORCID: 0000-0003-1434-5520
Faculty of Technical Sciences
University of Warmia and Mazury in Olsztyn
[2]Faculty of Technical Sciences
University of Warmia and Mazury in Olsztyn

Received 27 June 2019, accepted 17 October 2019, available online 28 October 2019.

K e y w o r d s: ram pump, drag force, CFD, ANSYS Fluent.

A b s t r a c t

The paper presents the results of a study investigating the equilibrium of forces acting on the closing element of the impulse valve in a water ram at the end of the acceleration stage. Acceleration is one of the three main stages in the working cycle of a water ram. In the first part of the paper, we estimated water velocity based on our earlier experimental measurements. We also calculated the minimum force required for closing the impulse valve. The second part of the paper discusses two variants of a numerical model, which was developed in ANSYS Fluent to determine the resultant hydrodynamic pressure and, consequently, the forces acting on the head of the impulse valve at the end of the acceleration stage. The main aim of this research was to verify the applicability of numerical modeling in water ram studies. The present study was motivated by the fact that Computational Fluid Dynamics is very rarely applied to water rams. In particular, we have not found any numerical studies related to the equilibrium of forces acting on the closing element of the impulse valve in a water ram.

Correspondence: Wojciech Sobieski, Katedra Mechaniki i Podstaw Konstrukcji Maszyn, Wydział Nauk Technicznych, Uniwersytet Warmińsko-Mazurski, ul. M. Oczapowskiego 11, 10-957 Olsztyn, phone +48 (89) 523 32 40, e-mail: wojciech.sobieski@uwm.edu.pl.

Introduction

A water ram is a pump which lifts water by relying on the energy of water flow. The pump can be supplied from any hydraulic source with a sufficient amount of water to guarantee a working fall. The minimum water head is approximately 1 m (MOHAMMED 2007, WATT 1975). This requirement has to be met to overcome friction forces (caused by water viscosity and turbulence), increase the flow rate of supply water and produce sufficiently large forces in the system.

Water flows freely through the working zone (zone *A*) of a water ram at the beginning of the cycle. The closing element (*4*) of the impulse valve (*3*) is in the down (open) position (Fig. 1). Water flows through an open impulse valve (*3*) and outside the ram pump into an evacuation channel or is indirectly fed to the source which supplies the ram. The Earth's gravity speeds up the flow of water in the working zone, thus increasing the hydrodynamic force acting on the closing element of the impulse valve (*4*). When the appropriate flow rate has been achieved, the hydrodynamic force exerted by water on the closing element of the impulse valve increases substantially and finally closes the valve (*Hydraulic ram pumps* 2019, *Water-powered* water… 2019, Meribah Ram Pump 2019, SHEIKH et al. 2013). The sudden cessation of water flow in the working zone produces a positive water hammer (BERGANT et al. 2006, CHOON et al. 2012, GHIDAOUI et al. 2005). The maximum pressure during water hammer is several or more than ten times higher than in the preceding phase (CHOON et al. 2012, GHIDAOUI et al. 2005, LANDAU, LIFSZYC 2009). The increase in pressure is determined mainly by the flow rate in the drive pipe, the rate of change in flow velocity, the stiffness of pump and drive pipe materials, and the amount

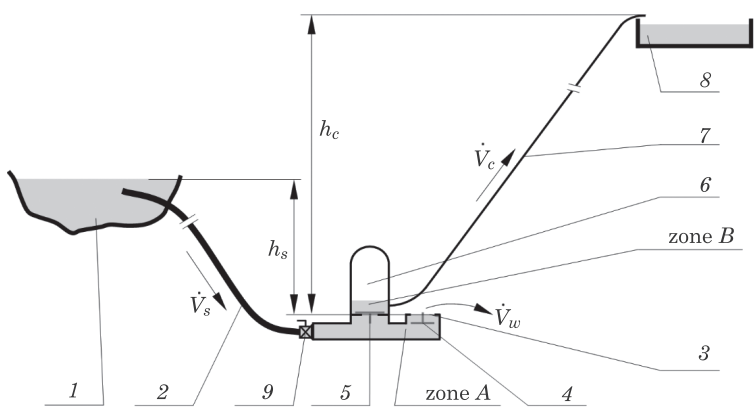

Fig. 1. Diagram of a water ram: *1* – water source, *2* – drive pipe, *3* – impulse valve, *4* – closing element of the impulse valve, *5* – pressure valve, *6* – air chamber, *7* – delivery pipe, *8* – water collector, *9* – shut-off valve, h_s – height of the water supply source, h_c – height of water outflow (delivery head), $\dot{V}_s$ – flow rate of water supply, $\dot{V}_c$ – rate of water outflow to the water collector, $\dot{V}_w$ – rate of water outflow to the surrounding environment; zone *A* – working zone, zone *B* – pressure zone; the impulse valve and the check valve are one-way (non-return) valves

of air in water (GRYBOŚ 1998, NAŁĘCZ, PIETKIEWICZ 2000a, 2000b). The resulting shock wave opens the pressure valve (*5*), and a certain amount of water enters the pressure zone (zone *B*). The pressure in the pressure zone increases after start-up, and it reaches a much higher level than the average pressure in the working zone. Pressure in the pressure zone is determined by delivery head (h_c). The air chamber (*6*) in the pressure zone minimizes pressure fluctuations in the delivery system. The movement of water from zone *A* to zone *B* (upwards) does not last long because the system is not in equilibrium, and flow quickly subsides in the delivery pipe. The movement of water is suppressed by the gravitational force, and water begins to flow downwards in the direction of the water source supplying the ram. The closing element of the pressure valve is moved by flowing water, and the pressure valve is closed. The closure of the pressure valve in the working zone produces negative water hammer, which opens the impulse valve and marks the beginning of a new cycle in a water ram.

This article presents selected aspects of an extensive research study analyzing the processes that occur in a single water ram cycle (GRYGO 2018, GRYGO, SOBIESKI 2015a, 2015b, SOBIESKI et al. 2016). The efficiency of water rams was tested in various configurations. The results were processed statistically, and the identified relationships were presented as regression equations (GRYGO 2018). The present study relied on data from the main stage of experimental measurements. The analyzed configuration has been described previously in (SOBIESKI et al. 2016).

In this study, the Finite Volume Method was used to simulate the operation of a water ram in the acceleration stage (water flows through the impulse valve only in the acceleration stage) based on geometry and flow rates in the experimental test rig. It should also be noted that numerical investigations of water rams have been rarely described in the literature. One of such studies was conducted by HARITH et al. (2017), but we cannot directly refer to their findings due to different research objectives and water ram constructions. Maw and HTET (2014) performed a simple analysis of pressure and velocity distribution in a water ram with the use of Solid Work software, but they did not discuss the equilibrium of the impulse valve. A similar study, performed using the Fluent code, was presented by SHENDE et al. (2015). However, the scientific merit of this study is relatively since the authors reported numerous results followed by a very brief (2-page) discussion. VERSPUY and TIJSSELING (1993) described the operation of a water ram, but they did not use the tools of Computational Fluid Dynamics (CFD) and instead relied on an analytical model based on the standard water hammer theory. Yet another model was presented by TIJSSELING and BERGANT (2012). However, the authors did not focus on water rams but on water hammer phenomena in a system of three connected reservoirs. One of the most advanced models was described by FILIPAN et al. (2003) who, however, used self-developed software instead of CFD tools.

Test stand

The test stand was composed of (Fig. 2): ¾ in drive pipe with the length of 7 m (*1*); ½ in delivery pipe (*2*); a welded ½ in steel pipe which constitutes the body of the water ram (*3*); air chamber (*4*) made of a PE pipe with a diameter of 65 mm, wall thickness of 4 mm and chamber volume of 1 dm^3, closed with plugs (*5*); one-way brass ½ in impulse valve (*6*) without spring retainers; one-way brass ½ in valve (*7*); connectors (*8*) for electronic pressure transducers (*9*); ball valve (*10*) for starting up the water ram; ball valve (*11*) for cutting off the delivery pipe; ball valve (*12*) for evacuating water from the delivery pipe.

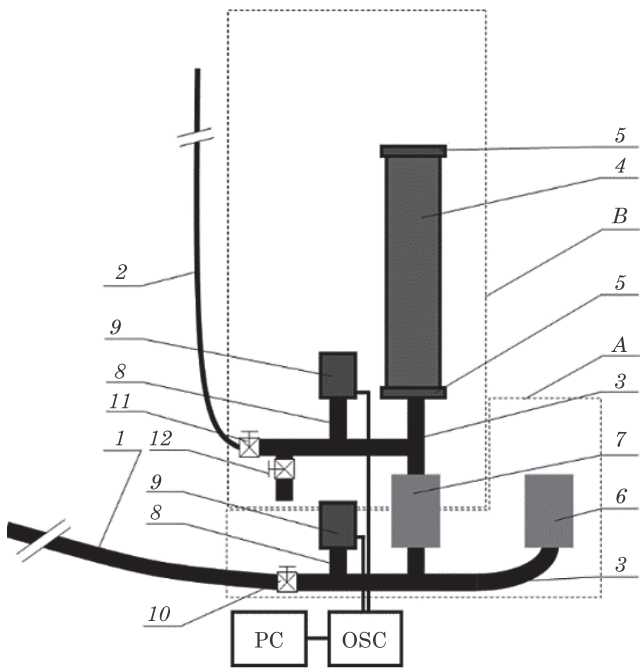

Fig. 2. Diagram of the experimental installation

The water ram was shut off for more than ten minutes before the measurements. Water head in the supply source and the height of the water tank were determined with a laser level and measuring tape. The experiment was conducted in a system with h_s = 4.96 m and h_c = 16 m. The pressure measurement system was checked. Changes in pressure were recorded with the EZ Digital DS-1080C laboratory oscilloscope with 80 MHz bandwidth and 100 MSa/s sample rate per channel, and Wika Model A-10 electronic pressure transducers. The time base was set at 0.02 to 0.1 s, and sensitivity – at 0.2 to 2 V.

Analysis of experimental data

The experimental stage has been described in detail by (SOBIESKI et al. 2016) and (GRYGO 2018). In this section, we estimated water velocity at the end of the acceleration stage needed to defining the boundary conditions in the numerical model. We also calculated the minimum force required for closing the impulse valve.

Changes in pressure in two zones of the water ram during a single working cycle are presented in Figure 3. The top line (denoted by number 1) represents changes in pressure in the working zone (*A*), and the bottom line (denoted by number 2) represents changes in pressure in the pressure zone (*B*). The duration of a single water ram cycle and the acceleration stage is indicated in the diagram.

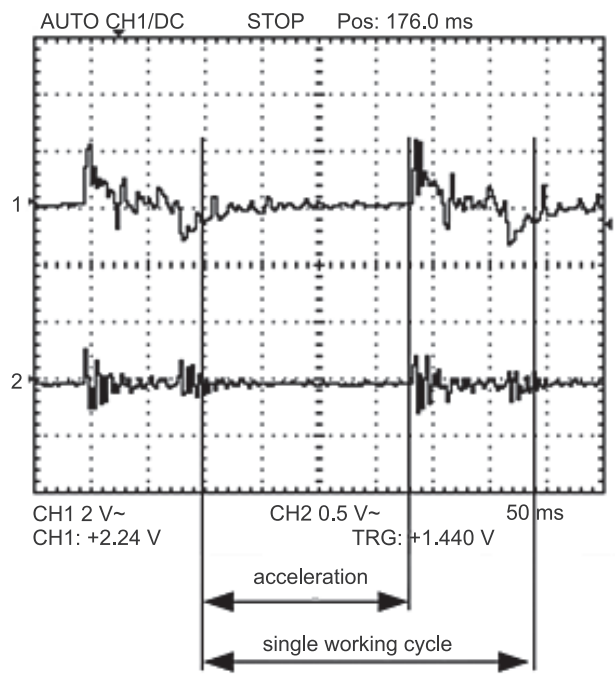

Fig. 3. Changes in pressure during a single working cycle of a water ram

The results of the experimental measurements indicate that 14 dm^3 of water flowed through the impulse valve and that the water ram completed 617.4 cycles in 3 minutes on average. TACKE (1998) reported that depending on supply head, waste valve adjustment and, to a lesser degree, on drive pipe length and delivery head, the cycle is repeated with a frequency of around 30 to 150 times per minute.

In our study, the above frequency was higher due to the fact that TACKE (1998) used massive industrial water rams whereas we used a small pump composed of typical hydraulic components. Another reason could be that the ratio between the height of the water supply source and the length of the delivery pipe was relatively small. However, the relevant data were not available and we could not evaluate the impact of this ratio on the operation of the water ram. Effective flow rate was determined at 0.00007777 m^3/s. Effective flow rate is the flow rate determined based on the total time of the measurement. The actual flow rate is higher because the acceleration stage is shorter than a single working cycle (207 ms) (SOBIESKI et al. 2016). Therefore, when the impulse valve is open, flow rate over time should be calculated with the use of the below formula:

$$\dot{V}_a = \frac{V}{t \cdot X_a} \tag{1}$$

where:

$\dot{V}_a$ – volumetric flow rate in the impulse valve in the acceleration stage [m^3/s],
V – volume of water flowing through the impulse valve during the measurement [m^3],
t – duration of measurement [s],
X_a – ratio of the duration of the acceleration stage to the duration of a single working cycle (0.7055 in the analyzed case).

For the measured data, $\dot{V}_a$ = 0.00010954 m^3/s.

The average water velocity in the acceleration stage can be calculated based on the internal diameter of the impulse valve equal to 0.012 m.

$$c_a = \frac{4 \cdot \dot{V}_a}{\pi \cdot d^2} \tag{2}$$

The result is 0.873 m/s for the measured data.

The scenario described by formula (2) is presented graphically in Figure 4*a*. In this variant, the water flow rate is assumed to be constant when the impulse valve is open. In reality, the initial flow rate is zero, and it begins to increase gradually when the impulse valve is opened (acceleration stage). However, the exact nature of the observed changes could not be described due to the complex internal geometry of the impulse valve. The conducted measurements revealed that the water flow rate increases over time. The above is presented in Figure 4*b* on the assumption that water velocity increases in a linear fashion. To obtain the same flow rate for the same period of time:

$$\dot{V}_a = \int_0^{t_a} \dot{V}_1(t)\mathrm{d}t = \int_0^{t_a} \dot{V}_2(t)\mathrm{d}t \tag{3}$$

the maximum velocity has to be twice that calculated for the previous variant.

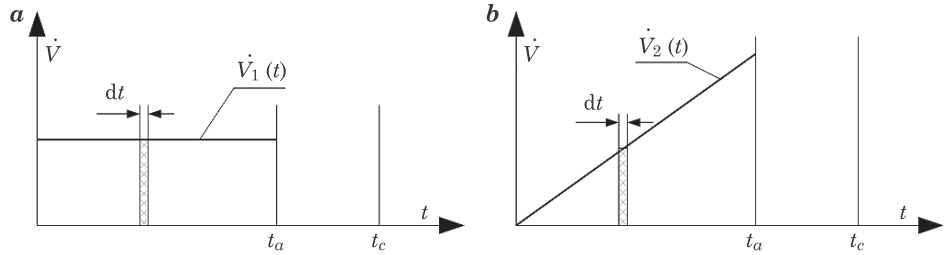

Fig. 4. Changes in flow rate over time: constant value (*a*) and increase (*b*)

Therefore:

$$c_{a,\max} = 2 \cdot c_a \tag{4}$$

where: $c_{a,\max}$ is the maximum velocity in the acceleration stage. This parameter was determined at 1.746 m/s for the measured values.

An analysis of the forces acting on the closing element of the impulse valve suggests that changes in valve position can be expressed as follows (*ANSYS Fluent in ANSYS…* 2012):

$$\vec{F}_a = \vec{a} \cdot \vec{F}_p + \vec{a} \cdot \vec{F}_v > \vec{G} \tag{5}$$

where:

$\vec{F}_a$ – resultant force in a given direction [N],
$\vec{a}$ – direction vector [–],
$\vec{F}_p$ – normal force (pressure) vector [N],
$\vec{F}_v$ – contact force (friction) vector [N],
$\vec{G}$ – weight force of the closing element of the impulse valve [N].

The closing element of the impulse valve applied in the experiment had a mass of 37.75 g, which is equivalent to the weight of 0.3703 N.

Numerical model

The Finite Volume Method was applied in numerical investigations. In this method, two main types of balance can be identified, namely surface balance and volumetric balance. The surface balance describes the possibility of exchanging a given physical quantity between the system and the surroundings via fluxes flowing through the surface of a Finite Volume. The volumetric balance describes the possibility of changing the balanced physical quantity within a Finite Volume.

The main set of balance equations may have the following form (SOBIESKI 2011):

$$\begin{cases} \dfrac{\partial \rho}{\partial t} + \operatorname{div}(\rho \vec{v}) = 0 \\ \dfrac{\partial (\rho \vec{v})}{\partial t} + \operatorname{div}\left(\rho \vec{v}\vec{v} + p\overleftrightarrow{I}\right) = \operatorname{div}(\overleftrightarrow{\tau}^{m} + \overleftrightarrow{\tau}^{\mathrm{R}}) + \rho s_b \\ \dfrac{\partial (\rho e)}{\partial t} + \operatorname{div}\left(\rho e \vec{v} + p\overleftrightarrow{I}\vec{v}\right) = \operatorname{div}[(\overleftrightarrow{\tau}^{m} + \overleftrightarrow{\tau}^{\mathrm{R}})\vec{v} + \vec{q}^{m} + \vec{q}^{\mathrm{R}}] + \rho s_e \end{cases} \tag{6}$$

where:

ρ – density [kg/m^3],
$\vec{v}$ – velocity [m/s],
p – static pressure [Pa],
$\overleftrightarrow{I}$ – unit tensor [–],
$\overleftrightarrow{\tau}^{m}$ – viscous molecular stress tensor [Pa],
$\overleftrightarrow{\tau}^{\mathrm{R}}$ – turbulent Reynolds stress tensor [Pa],
s_b – source of unitary mass forces [N/kg],
e – sum of kinetic and internal energy [N/(kg s)],
$\vec{q}^{m}$ – molecular heat flux [J/(m^2·s)],
$\vec{q}^{\mathrm{R}}$ – turbulent heat flux [J/(m^2·s)],
s_e – sources of heat [J/(m^3·s)].

The set of balance (or transport) equations (6) is not complied and needs to be supplemented by many "closures", which means that specific models describe individual problems (SOBIESKI 2013).

To develop a model simulating water flow through the impulse valve, the geometry of computational space has to be defined, a numerical grid has to be generated, boundary and initial conditions have to be defined, and the appropriate methods for solving numerical problems have to be selected.

The impulse valve was removed and disassembled to collect information about system geometry. All parts and dimensions were measured with an electronic caliper with a rated accuracy of 0.02 mm. System geometry and the numerical grid representing areas of water flow inside the valve are presented in Figure 5. The model was developed in the ANSYS v. 14.5 package (*Design Modeler User's Guide*… 2012, *ANSYS Fluent Meshing*… 2012, *ANSYS Fluent User's Guide*… 2012). All components of the closing element of the impulse valve (marked with different colors in Figure 5*a*) were grouped and given a collective name. This approach facilitated the calculation of the resultant normal and contact forces acting on all components of the closing element. It should also be noted that the valve's axis of symmetry was aligned with the *Y*-axis in the adopted system of coordinates. The rotation of the axis of symmetry denotes the direction of water flow (this axis is not presented in Figure 5, but it is shown in successive figures).

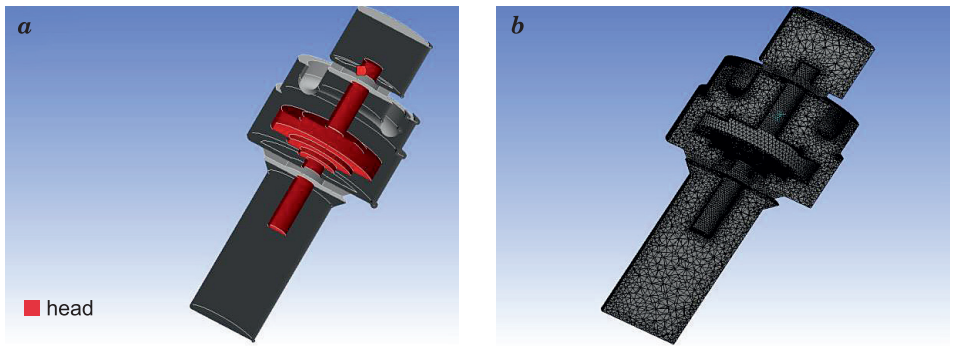

Fig. 5. Area of water flow inside the impulse valve: geometry (*a*) and the numerical grid (*b*)

The boundary and initial conditions of the numerical model were defined based on the experimentally measured values, and two variants were analyzed. The first variant involves a velocity inlet (boundary condition based on velocity; pressure is calculated during the simulation), and the second variant involves a pressure inlet (boundary condition based on pressure; velocity is calculated during the simulation). In the first variant, inlet velocity was the maximum velocity calculated with formula (4). This approach was adopted to analyze the situation in the system at the end of the acceleration stage. In the second variant, total pressure (p_t) was total static pressure resulting from water head in the supply source and dynamic pressure calculated for the maximum velocity:

$$p_t = \rho \cdot g \cdot h_s + \frac{\rho \cdot c_{a,\max}^2}{2} \tag{7}$$

which produces 50,138 Pa for the experimental values (dynamic pressure equals 1,523 Pa). In both variants, the pressure boundary condition at the inlet was equal to 101,325 Pa.

The parameters of the simulation model are presented in Table 1. All settings that did not result directly from the experimental data were assigned default values (*Theory Guide. Release 14.5*. 2012, *Tutorial Guide. Release 14.5*. 2012). This approach is recommended for modeling the flow of single-component fluids. Default values were also applied because turbulence parameters were unknown. The relevant measurements could not be performed during the experiment.

The distribution of total pressure on the closing element of the impulse valve in both variants is presented in Figure 6. The closing element is symmetrical, but four areas of higher pressure can be identified. The above can be attributed to the presence of guides that control the closing elements of the impulse valve. The guides separate the water stream in the top segment and cause macro-turbulence and micro-turbulence. Local pressure drops occur behind the guides, and the pressure on the closing element is highest in areas where water flow is unobstructed.

Table 1.

Parameters of the simulation model

No.	Parameter	Variant 1	Variant 2
1	Solver type	pressure based	
2	Velocity formulation	absolute	
3	Time	steady	
4	Gravity	-9.81 m/s^2 (in relation to *Y*-axis)	
5	Energy equation	off	
6	Viscous model	k-ε standard with standard wall function	
7	Water density	999.13 kg/m^3	
8	Viscosity	0.001003 kg/m·s	
9	Inlet velocity	1.746 m/s	-
10	Inlet initial gauge pressure	-	50,138 Pa
11	Inlet dynamic pressure	-	1,523 Pa
12	Turbulent intensity	5%	
13	Turbulent Viscosity Ratio	10	
14	Outlet pressure	101,325 Pa	
15	Turbulent intensity	5%	
16	Turbulent Viscosity Ratio	10	

Fluid velocity increases in valve grooves (Fig. 7). Local velocity is much higher than the average velocity calculated in the previous section. The option of calculating complete pressure and velocity fields is an unquestioned advantage of numerical modeling, and these values cannot be derived with the use of analytical methods. It should also be noted that the method of defining the inlet significantly influences fluid velocity in the entire computational area, and higher values were noted in variant 2.

Path lines colored according to static pressure are presented in Figure 8.

Static pressure is calculated relative to the reference value of 101,325 Pa. Static pressure decreased in the valve from around 31,100 Pa (variant 1) or 50,100 Pa (variant 2) to around zero, i.e. to the reference value (atmospheric pressure). Minor areas of negative pressure can be observed locally behind flow obstructions. These areas are not presented in the figures, but they can be deduced from the range of values in the legend.

An analysis of pressure and velocity values in the computational area indicates that velocity is adequate in variant 1 (velocity was input directly), whereas pressure in the top segment is too low. In variant 2, pressure is adequate (pressure was input directly), whereas velocity appears to be too high. Based on the experimental data, variant 1 seems to be a better option.

After numerical simulations, the resultant force acting on the closing element of the impulse valve in the direction of the Y-axis was calculated (the appropriate tool can be found in ANSYS Fluent). Under the simulated conditions, the resultant force was determined at 0.79 N in variant 1 and 1.32 N in variant 2. The resultant force is higher in variant 2 due to higher fluid velocity than in variant 1.

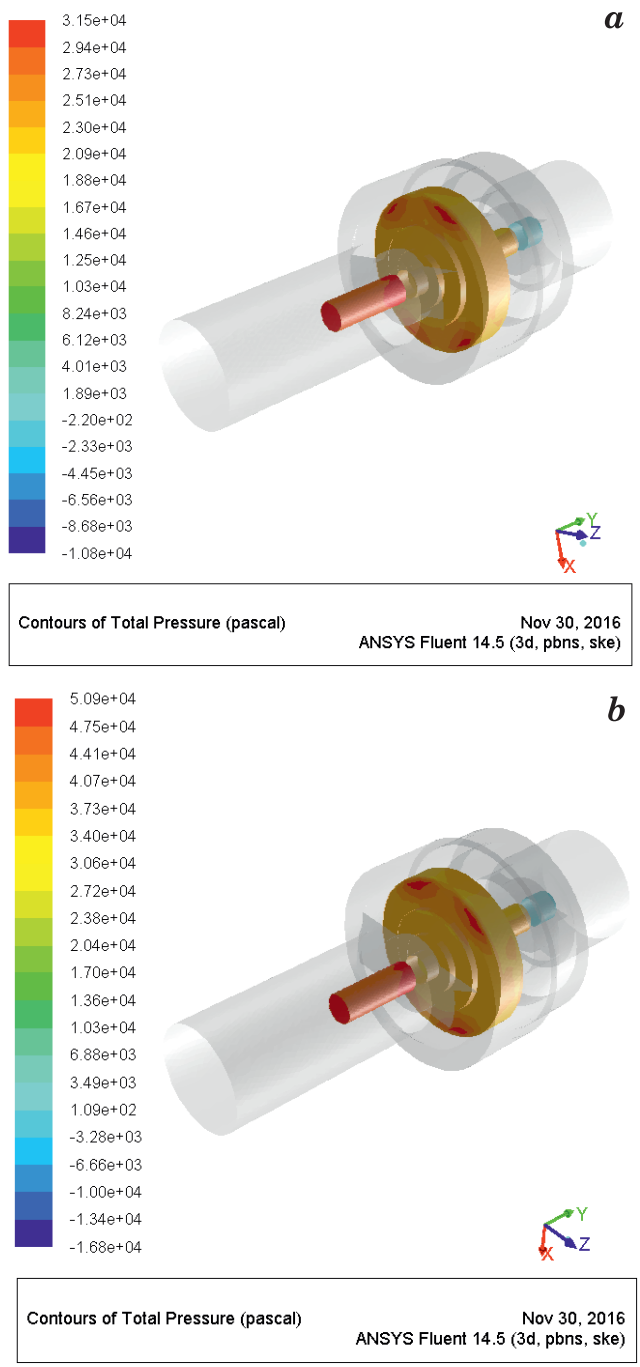

Fig. 6. Distribution of total pressure on the head of the impulse valve in variant 1 (*a*) and variant 2 (*b*)

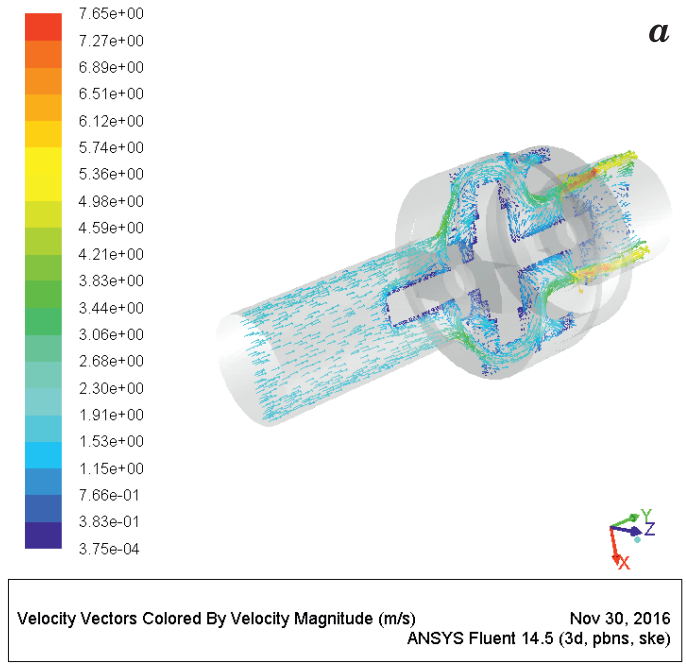

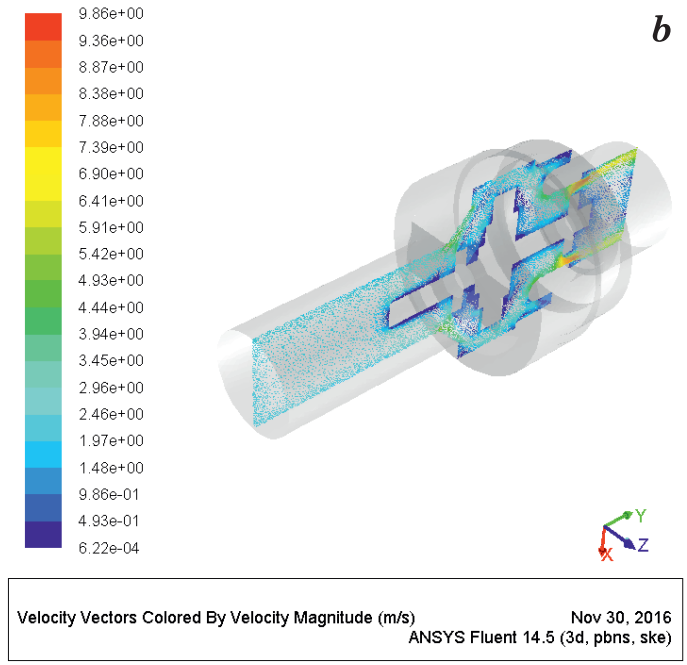

Fig. 7. Velocity fields for selected longitudinal cross-sections of the impulse valve in variant 1 (*a*) and variant 2 (*b*)

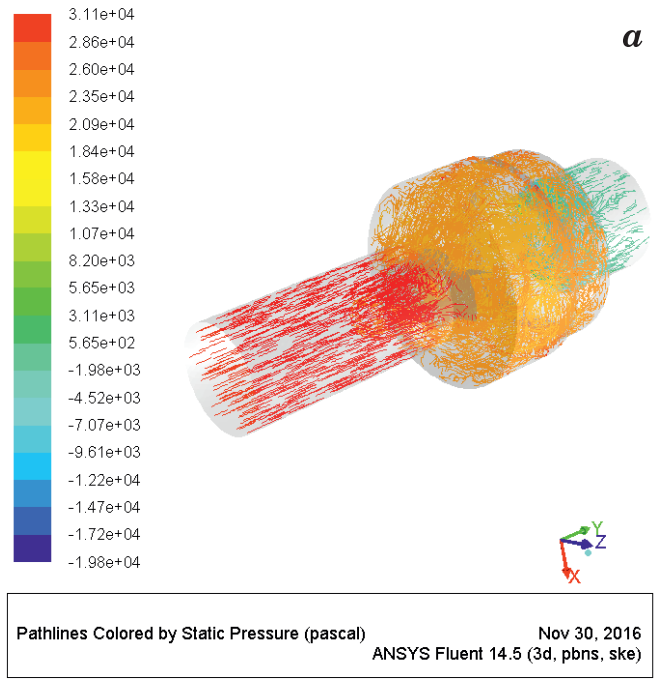

Fig. 8. Path lines colored according to pressure in variant 1 (*a*) and variant 2 (*b*)

The calculated interaction forces exceeded the weight of the impulse valve head 2.13-fold (variant 1) and 3.55-fold (variant 2). The above implies that the balance of forces at time t_a should be sufficient to close the valve. It should also be noted that time t_a marks the end of the acceleration stage which, as described in a previous study (SOBIESKI et al. 2016), is composed of three phases during which the impulse valve begins to open, the impulse valve is open, and the impulse valve begins to close. Therefore, interaction forces and the weight of the valve head were equalized earlier, i.e. before time t_a.

Summary

The following conclusions can be formulated based on the results of the present study:

- Numerical tools for fluid mechanics can be used to calculate the forces acting on selected elements that obstruct fluid flow, including the closing element of the impulse valve in a water ram pump. These tools can be applied to design new types of impulse valves that close faster (have a lower value of coefficient X_a) and, consequently, increase system efficiency.
- Numerical simulations produce higher values of interaction forces between flowing water and the closing element of the impulse valve than simple estimations (whose reliability is limited due to oversimplification). However, the degree of consistency between the simulation model and the experimental data is difficult to assess because in a real-world system, the closing element of the impulse valve begins to close before time t_a, and water flowing during valve closure can still accelerate and increase the force acting on the closing element of the impulse valve.
- The experimental data indicate that average fluid velocity (which is a key parameter in the defined model) should be calculated and that a velocity inlet should be incorporated in the numerical model.
- The scope of numerical analyses should be expanded in the future by evaluating the impact of the adopted turbulence model (and its parameters) on pressure values.

References

ANSYS Fluent in ANSYS Workbench User's Guide. Release 14.5. 2012. ANSYS Inc.
ANSYS Fluent Meshing User's Guide. Release 14.5. 2012. ANSYS Inc.
ANSYS Fluent User's Guide. Release 14.5. 2012. ANSYS Inc.
BERGANT A., SIMPSON A.R., TIJSSELING A.S. 2006. *Water hammer with column separation: A historical review*. Journal of Fluids and Structures, 22: 135-171.

CHOON T.W., AIK L.K., AIK L.E., HIM T.T. 2012. *Investigation of Water Hammer Effect Through Pipeline System*. International Journal on Advanced Science Engineering Informational Technology, 2(3): 48-53.

Design Modeler User's Guide. Release 14.5. 2012. ANSYS Inc.

FILIPAN V., VIRAG Z., BERGANT A. 2003. *Mathematical modelling of a hydraulic ram pump system*. Journal of Mechanical Engineering (Strojniški vestnik), 49(3): 137-149.

GHIDAOUI M.S., ZHAO M., MCINNIS D.A., AXWORTHY D.H. 2005. *A Review of Water Hammer Theory and Practice*. Applied Mechanics Reviews, 58: 49-76.

GRYBOŚ R. 1998. *Fundamentals of fluid mechanics*. PWN, Warszawa.

GRYGO D. 2018. *Analysis of the phenomena occurring during the water ram operation*. PhD Thesis, University of Warmia and Mazury in Olsztyn, The Faculty of Technical Sciences, Olsztyn.

GRYGO D., SOBIESKI W. 2015a. *Position of laboratory to phenomena research running in the ram water*. Mechanik, 7: 237-244.

GRYGO D., SOBIESKI W. 2015b. *Proposals to use hydraulic rams*. Woda-Środowisko-Obszary Wiejskie, 15: 31-47.

HARITH M.N., BAKAR R.A., RAMASAMY D., QUANJIN M. 2017. *A significant effect on flow analysis & simulation study of improve design hydraulic pump*. 4th International Conference on Mechanical Engineering Research (ICMER 2017). doi:10.1088/1757-899X/257/1/012076.

Hydraulic ram pumps. 2019. Appropedia. http://www.appropedia.org/Hydraulic_ram_pumps (February 28, 2019).

LANDAU L., LIFSZYC J. 2009. *Hydrodynamics*. PWN, Warszawa.

MAW Y.Y., HTET Z.M. 2014. *Design of 15 meter Head Hydraulic Ram Pump*. International Journal of Scientific Engineering and Technology Research, 3(10): 2177-2181.

MOHAMMED S.N. 2007. *Design and Construction of a Hydraulic Ram Pump*. Leonardo Electronic Journal of Practices and Technologies. 11: 59-70.

NAŁĘCZ T., PIETKIEWICZ P. 2000a. *Influence of air as the second phase for the velocity propagation of shock wave into multilayer pipe*. XVIII Conference of Research, Design, Production and Operating of Hydraulic Systems, Cylinder, Szczyrk.

NAŁĘCZ T., PIETKIEWICZ P. 2000b. *Determining of the velocity of the propagation impact wave into hydraulic lines with taking into account air as second phase*. XII National Conference Pneuma, Kielce, p. 255-262.

SHEIKH S., HANDA C.C., NINAEW A.P. 2013. *Design methodology for hydraulic ram pump (hydram)*. International Journal of Mechanical Engineering and Robotics Research, 2(4): 170-175.

SHENDE P. B., CHOUDHARY S.K., NINAWE A.P. 2015. *Analysis and Enhancement of Hydraulic Ram Pump using Computational Fluid Dynamics (CFD)*. International Journal for Innovative Research in Science & Technology, 2(3): 2349-6010.

SOBIESKI W. 2011. *The basic equations of fluid mechanics in form characteristic of the finite volume method*. Technical Sciences, 14(2): 299-313.

SOBIESKI W. 2013. *The basic closures of fluid mechanics in form characteristic for the Finite Volume Method*. Technical Sciences, 16(2): 93-107.

SOBIESKI W., GRYGO D., LIPIŃSKI S. 2016. *Measurement and analysis of the water hammer in ram pump*. Sadhana, 41(11).

TACKE J.H.P.M. 1988. *Hydraulic rams – a comparative investigation*. Communications on Hydraulic and Geotechnical Engineering, Delft University of Technology, Faculty of Civil Engineering, Report 88-1, ISSN 0169-6548. http://repository.tudelft.nl/.

Theory Guide. Release 14.5. 2012. ANSYS Inc.

TIJSSELING A.S., BERGANT A. 2012. *Exact computation of waterhammer in a three-reservoir system*. CASA-Report 12-41, December 2012, Eindhoven University of Technology, The Netherlands.

Tutorial Guide. Release 14.5. 2012. ANSYS Inc.

VERSPUY C., TIJSSELING A.S. 1993. *Hydraulic ram analysis*. IAHR Journal of Hydraulic Research, 31: 267-278.

Water-powered water pumping systems for livestock watering. 2019. Canada Agriculture and Agri-Food. http://www1.agric.gov.ab.ca/$department/deptdocs.nsf/ba3468a2a8681f69872569d60073fde1/42131e74693dcd01872572df00629626/$FILE/wpower.pdf (February 28, 2019).

WATT S.B. 1975. *A manual on the hydraulic ram for pumping water*. Intermediate Technology Development Group, Water Development Unit, National College of Agricultural Engineering, Bedford.

Why Meribah Ram Pump? 2019. Meribah Ram Pump. https://www.meribah-ram-pump.com/ (January 8, 2019).

Technical Sciences, 2019, 22(3), 221–235

UNIWERSYTET WARMIŃSKO-MAZURSKI W OLSZTYNIE

Quarterly peer-reviewed scientific journal
ISSN 1505-4675
e-ISSN 2083-4527
TECHNICAL SCIENCES
Homepage: www.uwm.edu.pl/techsci/

doi: 10.31648/ts.4966

WEAR ANALYSIS OF A GUN BARREL DRILL BLADE IN 1.0503 STEEL DRILLING PROCESS IN MILPRO HG12 OIL ENVIRONMENT WITH THE ADDITION OF ULTRA-DISPERSIVE COPPER PARTICLES AND COPPER OXIDES

***Kazimierz Rychlik*[1], *Cezary Senderowski*[2]**

[1]ORCID: 0000-0003-2978-4681
Research Network ŁUKASIEWICZ – Institute of Mechanized Construction and Rock Mining Warszawa
[2]ORCID: 0000-0002-0331-3702
Department of Material and Machine Technology
University of Warmia and Mazury in Olsztyn

Received 13 October 2019, accepted 4 December 2019, available online 17 December 2019.

K e y w o r d s: barrel drill, deep hole drilling, long holes.

A b s t r a c t

This paper presents structural solutions for guiding a single-sharp barrel drill blade during deep hole drilling, and it analyzes the structural and technological problems associated with two modes of inserting the drill into the processed material in the first stage of drilling – with the use of a pilot hole or a guide sleeve.

The kinematics of the object-tool system (P-N) and other technological parameters affecting the execution of pilot holes under strictly defined conditions were analyzed during deep drilling with barrel drills in the FNE 40NC AVIA vertical numerical milling machine.

Performance tests involving two types of cooling-lubricating agents, Milpro HG12 oil with and without the addition of ultra-dispersive copper particles and copper oxides (0.05 ÷ 0.6 μm) and Panther GP-1 additive (PWPH PantherOil Poland), applied in a 1:100 ratio, were described.

The wear of the barrel drill blade along the entire drilling path (Lw = 8,000 mm) for 112 holes, and the geometric wear coefficient K_w of the drill bit were determined in 1.0503 steel with the use of EB80 drills made of K15 cemented carbide (WC 94%, Co 6%) with a diameter Dc = 8 mm.

Correspondence: Kazimierz Rychlik, Research Network ŁUKASIEWICZ – Institute of Mechanized Construction and Rock Mining, Racjonalizacji 6/8, 02-673 Warszawa, phone: +48 22 853 21 77, e-mail: k.rychlik@imbigs.pl

The results of wear tests were compared with the results of tribological tests involving cooling lubricants and 1.0503 steel with the chemical composition of K15 tungsten carbide. The abrasive wear of friction pair and the performance of the barrel drill blade during deep hole drilling were analyzed under identical conditions.

Introduction

Deep hole drilling in machining operations is influenced by the method of drilling holes whose depth (length) exceeds hole diameter five-fold (GÓRSKI 1961, STREUBEL 1993, RYCHLIK 2010). The following characteristics of the deep hole drilling technology have to be analyzed:

– cutting tool design,

– working parameters of the tool, in particular the type and parameters of the applied coolants (cooling and lubricating agents),

– the configuration of specialist machinery for implementing the deep hole drilling technology.

Deep hole drilling operations can be divided into two main groups based on the manner in which the material is processed into chips (GÓRSKI 1961, GÓRSKI 1990) – Figure 1.

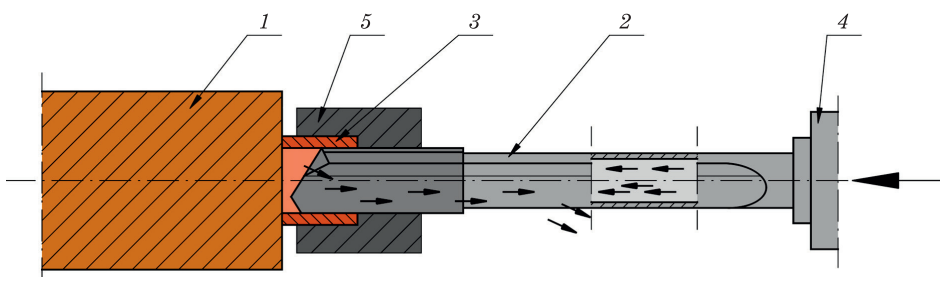

Fig. 1. Guiding a barrel drill with a pilot sleeve: *1* – workpiece, *2* – drill, *3* – drill guide (pilot sleeve), *4* – tool holder, *5* – steady rest

The guide sleeve of a barrel drill works in harsh conditions because each time it enters and exits the workpiece, it comes into contact with the tool blade and chips. For this reason, sleeve material should be highly resistant to wear. Most guide bushes are made of K15 sintered carbide which is characterized by sufficient durability. However, sintered carbide guide bushes are expensive due to a difficult machining process. The authors' experience indicates that only several holes can be drilled with the use of high-speed steel sleeves because the guide sleeve hole has to be calibrated. Guide sleeves made of H10 carbide have superior mechanical properties. Drill guide bushings should be manufactured with high accuracy because they significantly influence drilling precision

(not only at the point of the tool's entry into the material, but also along the entire drilling path). Drill guide bushing also acts as a sealing lubricant and a base in the axial direction of the workpiece. The axial homing of the workpiece is particularly important when drilling depth is strictly determined by technological requirements.

Guide bushing generally does not come into contact with the workpiece when the hole is drilled and the drill is inserted an an angle. The authors' experience indicates that the gap between the workpiece and the sleeve should not exceed 0.1 mm (RYCHLIK 2010). When the gap is too large:

– the drill entry point is displaced, which increases the straightness error of the drill hole at the exit,

– additional oil mist is formed, and it is difficult to remove from the machining chamber,

– the evacuated chip gap is jammed.

In the second drilling method, the drill is inserted into the workpiece using a pilot hole (Fig. 2). In this approach, a pre-drilled hole with diameter $D_c^{+0.03}$ should be made to a depth of approx. 1÷1.5 D_c. This method usually requires a CNC machining center. The main limitation of this approach is the depth of the drilled hole due to the difficulties associated with the use of supports and the reduced distance between the spindle face and the machining chuck (table). These limitations apply mainly to vertical machining centers.

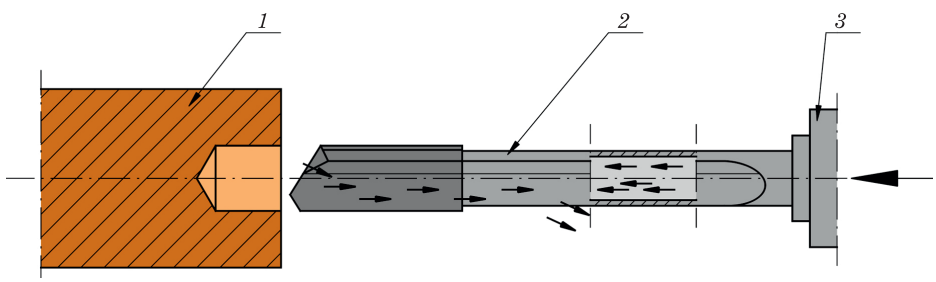

Fig. 2. Guiding a barrel drill through a pilot hole: *1* – workpiece, *2* – drill, *3* – tool holder

The results of wear tests involving H10 sintered carbide and K15 tungsten carbide barrel drills were analyzed in view of the processing requirements for deep hole drilling as well as the structural properties and the behavior of the tested materials. The wear behavior of the examined materials was examined during laboratory tests of H10 sintered carbide and K15 barrel drills. The impact of the applied lubricants on the progression of wear was described, and the friction coefficient and the geometric wear coefficient K_w of the barrel drill blade were determined in accordance with Standard PN-83/M-58350.

Materials and Methods

The study involved tribological and performance tests to determine:
– material resistance to abrasive wear using the pin-on-disc method,
– the wear of single-edge barrel drills during hole drilling.

Material resistance to abrasive wear was tested with the use of the pin-on-disc method on H10 sintered carbide substrate. The physicochemical properties of H10 sintered carbide are presented in Table 1. Sample dimensions are presented in Figure 3.

Table 1

Physicochemical properties of the substrate material for tribological tests and performance tests (barrel drill blades)

Parameter	Manufacturer's specifications (BAILDONIT)
Type of material	Sintered carbide
Type	H10
Chemical composition	WC 94%, Co 6%
Density	14.85 g/cm^3
Grain size	1.0 ÷ 2.0 μm
Hardness HV30	1,600

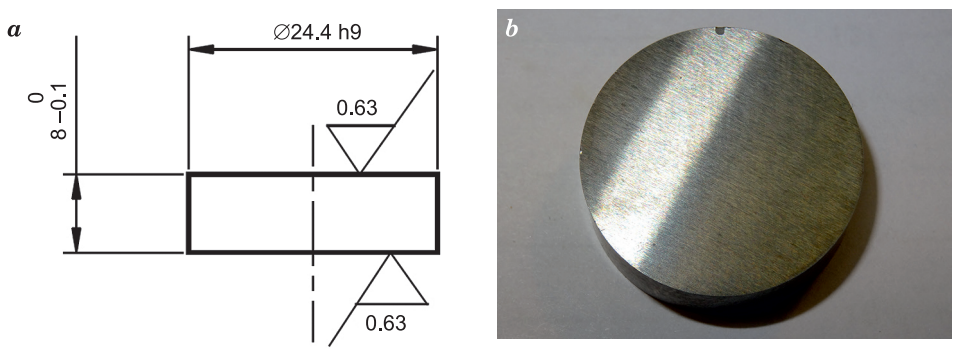

Fig. 3. Substrate material for tribological tests: *a* – schematic diagram, *b* – substrate material (H10 sintered carbide). The properties of the substrate material are presented in Table 1

Commercial H10 carbide for the experiment was manufactured by Baildonit, and its chemical composition was identical to that of the K15 carbide barrel drill. H10 sintered carbide containing 6% Co (% wt.) is widely used in the production of cutting materials and plastic deformation tools due to high resistance to abrasive wear, very high hardness and mechanical strength, and superior cutting properties, in particular high resistance of the cutting edge to micro spalling and adhesive bonding at high temperatures. The functional properties

of WC-Co carbides are influenced by the size of WC grains and the admixture of Co, where the hardness of the material increases with a rise in the size of WC grains. In WC-Co carbides, fracture toughness increases with a rise in Co content, and hardness is maintained by the ductile Co matrix.

The counter specimens were 1.0503 hypereutectoid steel pins which are presented in Figure 4.

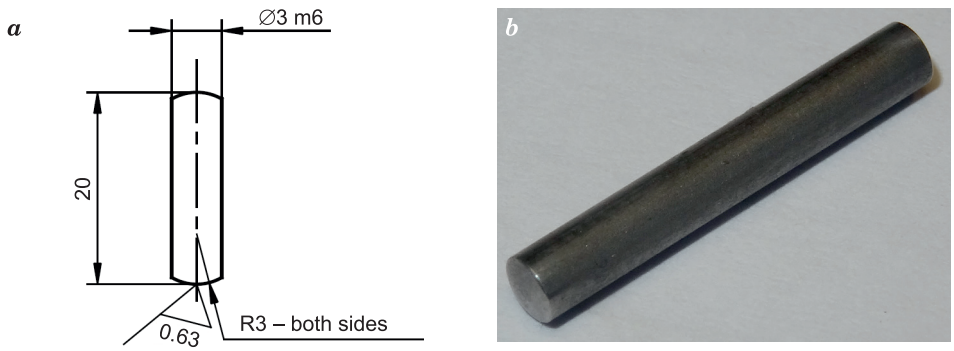

Fig. 4. Counter specimen – 1.0503 steel pin for pin-on-disc wear tests:
a – schematic diagram, *b* – steel pin

The friction coefficient and the wear of the friction pair were determined in abrasion resistance tests based on Standards ISO 20808: 2016; DIN 50324: 1992; PN-ISO 5725: 2002; ASTM G99 - 95.

The tests were carried out in the T-11 tribotester (Fig. 5) which assesses the tribological properties of sliding machine components such as lubricants and materials intended for operation at high temperatures.

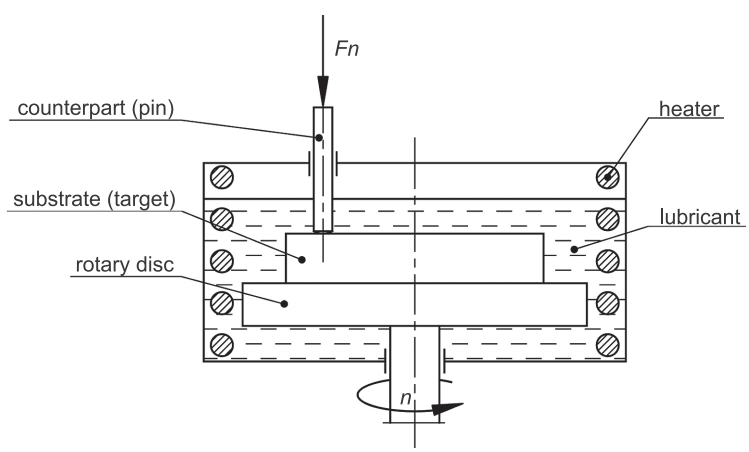

Fig. 5. Diagram of the T-11 tribotester chamber

In abrasion resistance tests, the friction pair comprised a stationary mandrel pressed with force F_n to a disk rotating with rotational speed n. The friction node was placed in an insulated thermal chamber with a heating element which heats the chamber and maintains a constant temperature of up to 300°C. Materials can also be tested in the chamber in a gas atmosphere. Changes in the friction force, linear wear and temperature at the point of contact between the elements at a given constant rotational speed of the disc were registered continuously by a digital control system to determine the time and path of friction in the test chamber. Abrasion resistance tests were carried out without and with Milpro HG12 oil, with and without the addition of Panther GP-1. Milpro HG12 oil is intended for grinding and machining under harsh conditions. It consists of deeply refined mineral oils, lubricants and EP/AW anti-wear and anti-seize additives. The properties of the applied oil are presented in Table 2.

Table 2

Specification of Milpro HG12 oil based on the product safety data sheet

Parameter	Value
Appearance	transparent
Color	yellow
Density at 15°C	859 kg/m^3
Viscosity at 40°C	12 mm^2/s
Ignition temperature	155°C
Copper corrosion	4B
Chlorine content	0%
Anti-fog properties	yes

Panther GP-1 concentrate (PWPH PantherOil Poland) formulated based on Valona MS 7023 oil and containing 10% of ultra-dispersive Cu and CuO particles (0.05 ÷ 0.6 mm) was used as an additive to decrease the friction coefficient. The concentrate was added to Milpro HG12 oil (1:100) in abrasive wear tests. Panther GP-1 concentrate forms microlayers with unique properties which improve the durability of the oil film during barrel drill cutting at high temperature and high unit load when the viscosity of the lubricating-cooling oil decreases.

Before the test, each sample was washed in acetone and dried in air. The parameters of abrasive wear tests in the T-11 tribotester are presented in Table 3.

Performance tests involved single-acting barrel drills (Fig. 6) manufactured by GÜHRING with cutting blades made of uncoated K15 material with identical properties to the H10 carbide substrate in tribological tests (Tab. 1).

The structural parameters of the drills are presented in Table 4.

Table 3

Parameters of tribological tests analyzing the wear resistance of H10 sintered carbide and 1.0503 steel friction pair in the T-11 tribotester

Parameter	Value
Type of motion	sliding motion
Contact geometry	pin-on-disc
Counterpart diameter (pin)	φ 3 mm with rounded face and radius of R3
Substrate diameter (target)	φ 25.4 mm
Rotational speed of the disc	95.5 rpm
Sliding velocity	0.1 m/s
Friction path	1,000 m
Number of cycles	15,923
Load	10 N
Fraction radius	10 mm
Temperature in the test chamber	23°C
Relative air humidity	52%
Reading recorded results	every 100 mm of the friction path

Table 4

Structural parameters of barrel drills with sintered K15 carbide blades used in performance tests

Parameter	Description
Drill type	EB80
Number of cutting edge	2 edges located asymmetrically relative to the tool rotation axis
Blade type	monolithic K15 carbide (uncoated)
Arrangement of work support blade	G-type
Convergence of work support blade	1:800
Drill shank	WHISTLE NOTCH (E – STANDARD)

Fig. 6. Single-blade barrel drill used in performance tests

The base unit of the test stand was the FNE 40NC AVIA vertical numerical milling machine with stepless adjustment of spindle speed in the range of 0÷4,000 rpm. The milling machine was equipped with a 5.5 kW vertical spindle and an ISO40 socket for hydraulic clamping of the tool holder. A horizontal table enabled pivoting movements in *X*/*Y*/*Z* directions to 620/420/400 mm, respectively. The cooling system comprised a 100 L oil tank and a hydraulic pump which supplied oil to the machining zone through the tool holder and the drill (pressure – 3 MPa, flow rate – 10 L/min).

The components of the tool kit used in field tests are presented in Table 5.

Table 5

Tool kit components used in performance tests

Component	Description
Working tool	EB80 barrel drill
Specialized modular holder with external coolant supply:	–
– holder	DIN2080 A40 OTT MHD63.60
– rotary joint	ACR63/63
– tool holder	AW63/20

To implement the deep hole drilling technology with the use of barrel drills, pilot holes for guiding the drill had to be made in the first phase of drilling. The pilot hole was drilled in four stages, as shown in Figure 7.

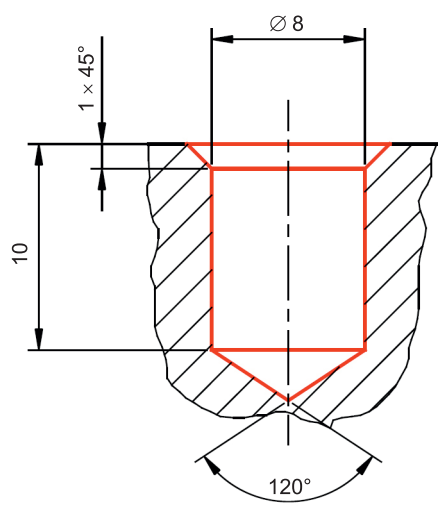

Fig. 7. Basic dimensions of the pilot hole

The following assumptions were made to determine the work cycle of the barrel drill in performance tests:

– the drill is inserted into the workpiece (PO) through a pilot hole,

– holes are drilled through,

– the accumulated chips have to be removed when drilling successive holes,

The technical parameters of drilling tests are presented in Table 6, and the operation of the barrel drill in performance tests is illustrated graphically in Figure 8.

Table 6

Technical parameters of deep hole drilling with barrel drills in performance tests

Parameter	Value
Rotational speed of drill, n	2,500 rpm
Drill feed rate, f_m	50 mm/min
Feed rate per drill tooth, f_z	0.02 mm
Cutting speed, V_c	62.8 m/min
Cooling lubricant	Milpro HG12 oil Panther GP-1 supplement
Oil pressure, P	3 MPa
Oil flow, Q	10 l/min

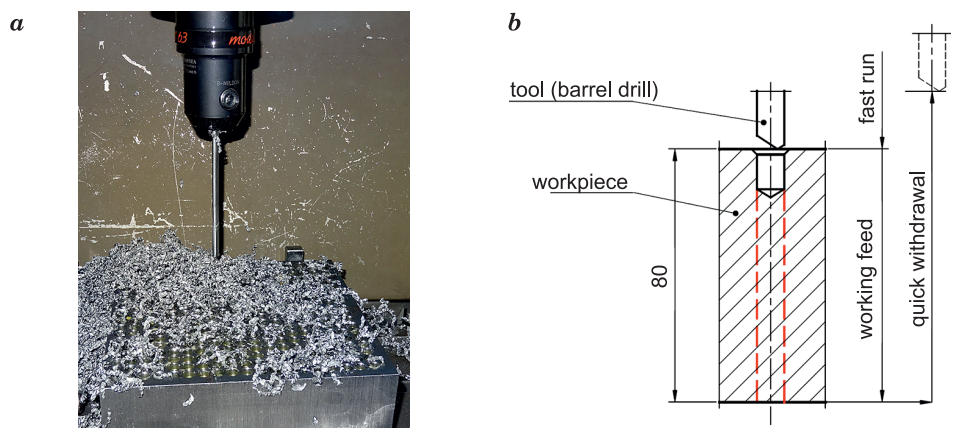

Fig. 8. The operation a single-blade barrel drill in the test stand: *a* – deep hole drilling, *b* – work cycle of the barrel drill

Plates made of 1.0503 steel, measuring 200 × 200 × 80 mm, were used in wear tests of barrel drill blades.

The wear of barrel drill bits at 14-hole intervals (LWO), which were equivalent to the drilling path L_w = 1,000 mm, was determined under OPTA-TECH MN800P and Levenhuk DTX 90 microscopes equipped with a measuring

and image recording system. The first measurement was made after drilling 28 holes (L_w = 2,000 mm). The total length of the drilling path for the analyzed tool-coolant-lubricant configuration was L_w = 8,000 mm, and it corresponded to 112 through holes. The measurements were used to determine the geometric wear coefficient K_W of the barrel drill according to Standard PN-83/M-58350.

Results and Discussion

Friction pair measurements (1.0503 steel and H10 cemented carbide) are presented in Tables 7 and 8 and are illustrated graphically in Figures 9 and 10.

Table 7

Friction measurements of the 1.0503 / H10 friction pair

Test	Coefficient of friction, μ	Average coefficient of friction, μ	Standard deviation
Dry run			
1	0.71209	0.63932	0.06602
2	0.61949		
3	0.54473		
4	0.69123		
5	0.62909		
Friction in Milpro HG12 oil environment			
1	0.12337	0.11744	0.00551
2	0.11646		
3	0.11249		
Friction in Milpro HG12 oil environment with Panther GP-1 additive			
1	0.10699	0.11281	0.00535
2	0.11392		
3	0.11751		

The results of 1.0503/H10 friction pair tests revealed that the average value of the friction coefficient (around m = 0.64) was highest in the dry run. When the friction pair was tested in the presence of Milpro HG12 oil (without the addition of Panther GP-1), the friction coefficient decreased by 81.6% to approximately M = 0.12. When both Milpro HG12 oil environment and Panther GP-1 lubricant were added to the test chamber, the friction coefficient increased by approximately 82.4% relative to the dry run. The application of Panther GP-1 lubricant with ultra-dispersive Cu and CuO particles with a diameter of 0.05 ÷ 0.6 μm decreased the viscous friction coefficient by around 4% (relative to pure Milpro HG12 oil) in the gap between the surfaces of co-acting elements.

Table 8

Cumulative results of wear tests involving the 1.0503/H10 friction pair

Test	Wear [μm/m]	Average wear [μm/m]	Standard deviation [μm]
Dry run			
1	0.96812	1.23463	0.20650
2	1.10251		
3	1.35549		
4	1.37352		
5	1.24195		
Friction in Milpro HG12 oil environment			
1	0.13737	0.13737	0.01593
2	0.10555		
3	0.12289		
Friction in Milpro HG12 oil environment with Panther GP-1 additive			
1	0.09108	0.09195	0.00123
2	0.09282		
3	0.10882		

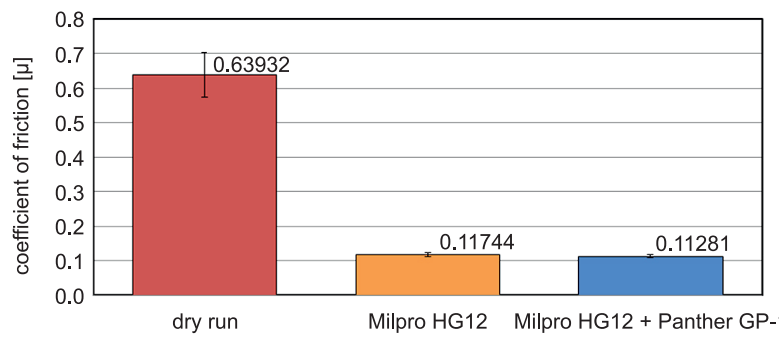

Fig. 9. Average values of the friction coefficient in the 1.0503/H10 friction pair

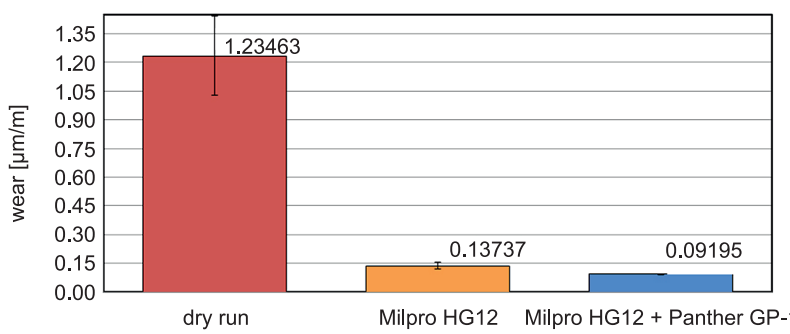

Fig. 10. The results of wear tests involving the 1.0503/H10 friction pair

Similarly to the friction coefficient μ, the highest wear (around 1.23 μm/m on average) of the 1.0503/H10 friction pair was noted in the dry run. Wear decreased by 88.8% to approximately 0.14 μm/m when Milpro HG12 oil was used without the addition of Panther GP-1. Wear decreased by approximately 92.6% when Milpro HG12 oil and Panther GP-1 lubricant were added to the test chamber. The friction coefficient decreased by around 4% because the friction surface was protected by a sublayer formed by Milpro HG12 lubricating oil with ultra-dispersion Cu and CuO particles (relative to Milpro HG12 lubricating oil applied alone), which decreased the wear of the tested friction pair by approximately 33%. The above can probably be attributed to the fact that ultra-dispersion Cu and CuO particles were able to rebuild the protective lubricating layer of Milpro HG12 oil under abrasive wear conditions.

In performance tests, the wear of the single-blade barrel drill was analyzed based on the wear of blade tip W in plane P_r, and it was expressed by the geometric wear coefficient K_W, as shown in the diagram in Figure 11. The results of performance test conducted under all drilling conditions with the use of specific lubricants (without dry runs) are presented in Table 9 and Figures 12 and 13.

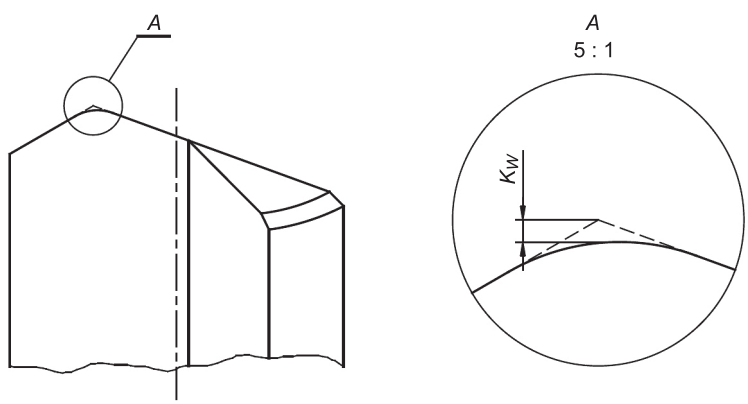

Fig. 11. Wear coefficient K_W of the single-blade barrel drill in plane Pr

The results of microscopic tests revealed that the tip W of the barrel drill bit was worn in plane P_r under the applied drilling conditions. After drilling (L_w = 8,000 mm; LWO = 112 through holes), tip wear was determined at K_w = 0.132 mm when the barrel drill was operated in the presence of Milpro HG10 oil without the addition of Panther GP-1. When Milpro HG12 oil was used in combination with the Panther GP-1 additive along the same drilling path L_w, the wear coefficient was determined at K_w = 0.087 mm, and it was more than 34% lower relative to the test involving pure Milpro HG12 oil.

The friction coefficient increases when the feed rate is reduced and the remaining machining parameters remain constant (BOGDAN-CHUDY, NIESŁONY 2015, FELDSHTEIN, MARUDA 2010). The obtained results indicate that drilling tests performed at a low feed rate per drill tooth (f_z = 0.02 mm) can significantly affect the friction coefficient. Unfortunately, the feed rate of barrel drills cannot be significantly increased due to design and strength constraints.

Table 9

The wear of the single-blade barrel drill expressed by the wear coefficient K_W

Measurement No.	Number of drilled holes LWO	Drilling path *Lw* [mm]	Wear coefficient K_W	
			Milpro HG12 oil [mm]	Milpro HG12 oil + Panther GP-1 additive [mm]
1.	28	2000	0.053	0.039
2.	42	3000	0.069	0.045
3.	56	4000	0.082	0.056
4.	70	5000	0.089	0.061
5.	84	6000	0.094	0.067
6.	98	7000	0.11	0.072
7.	112	8000	0.132	0.087

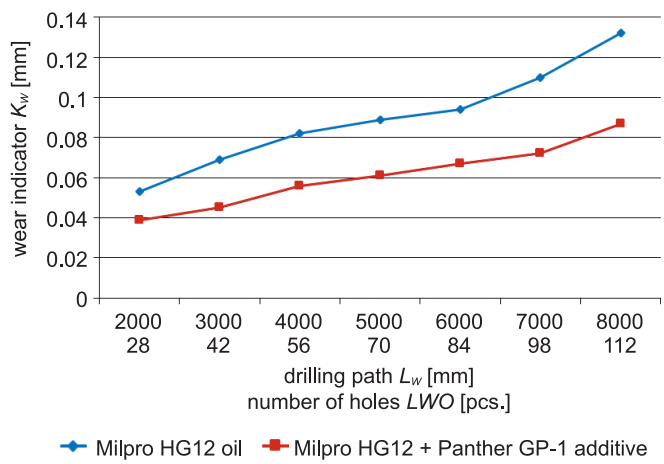

Fig. 12. Changes in the value of the wear coefficient K_W of the single-blade barrel drill as a function of the number of drilled holes, expressed by changes in the drilling path in performance tests conducted under all drilling conditions with the use of specific lubricants

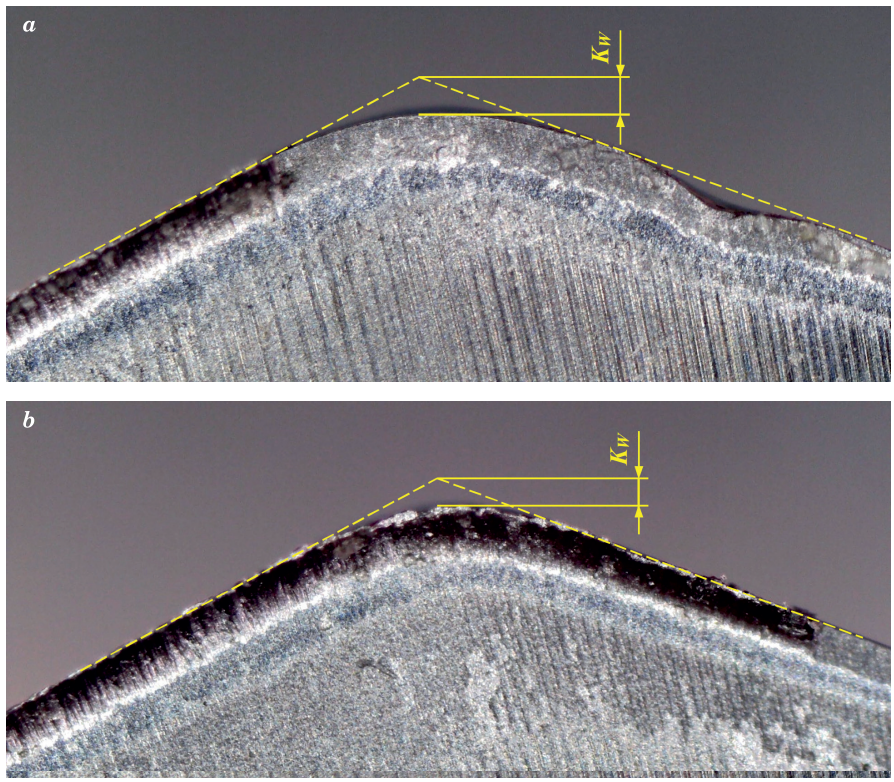

Fig. 13. Corner wear of the single-blade barrel drill at LWO = 112; *Lw* = 8,000 mm with oil: *a* – Milpro HG12, *b* – Milpro HG12 with Panther GP-1 additive

Conclusions

The results of the tribological tests of the C45 / H10 friction pair indicate that a decrease in the friction coefficient μ is accompanied by a decrease in wear during wet abrasion when a lubricant is used. In tests involving Milpro HG12 oil with Panther GP-1 additive, the wear of the tested friction pair decreased by more than 33%, and the friction coefficient μ decreased by approximately 4% relative to the values noted when pure Milpro HG12 oil was used. The performance tests of the barrel drill blade revealed considerable wear of the blade tip based on the calculated values of the geometric wear coefficient K_W. When 112 through holes were drilled along a path of 8000 mm, the application of Milpro HG12 oil with Panther GP-1 additive decreased tip wear by approximately 34%. Tribological and performance tests confirmed that the addition of Panther GP-1 lubricant to Milpro HG12 oil decreases the coefficient of friction μ and the linear wear of the material used in barrel drills.

Acknowledgements

The author would like to thank K. Ziewiecki, M.Sc., from the Eko-Tech Company for preparing the Panther GP-1 concentrate for tribological tests. The author is also grateful to A. Wojtkowiak from the University of Warmia and Mazury in Olsztyn, Poland, for critically revising the manuscript.

References

BOGDAN-CHUDY M., NIESŁONY P. 2015. *Ocena warunków tribologicznych podczas skrawania stopu inconel 718 płytką z węglika spiekanego*. Mechanik, 8-9: 91-97.

FELDSHTEIN E., MARUDA R. 2010. *Analiza warunków tarcia na powierzchni natarcia przy toczeniu wykończeniowym na podstawie zmian grubości wióra*. Tribologia, 4: 87-95.

GÓRSKI E. 1961. *Narzędzia do wiercenia i roztaczania głębokich otworów*. PWT, Warszawa.

GÓRSKI E. 1990. *Podstawy technologii uzbrojenia*. WPW, Warszawa.

JEMIELNIAK K. 2004.*Obróbka skrawaniem*. OWPW, Warszawa.

RYCHLIK K. 2008. *Technologia głębokiego wiercenia otworów wiertłami lufowymi w produkcji seryjnej*. VI Konferencja Naukowo-Techniczna *Technologia i organizacja produkcji seryjnej* – TIOPS 2008, Regietów.

RYCHLIK K. 2010. *Koncepcja technologii wiercenia głębokich otworów wiertłami lufowymi z zastosowaniem zmiennych parametrów skrawania*. (praca magisterska), Wydział Inżynierii Produkcji Politechniki Warszawskiej, Warszawa.

RYCHLIK K., JASTRZĘBSKI M., BRAMOWICZ M. 2011. *Problemy smarowania, chłodzenia i odwiórowania w technologii głębokiego wiercenia*. Technologia i Automatyzacja Montażu, 1, Warszawa.

STREUBEL A. 1993. *Obróbka długich otworów*. WPW, Wrocław.

Standards

Accuracy (correctness and precision) of measurement methods and measurement results. PN-ISO 5725: 2002.

Fine ceramics (advanced ceramics, advanced technical ceramics). Determination of friction and wear characteristics of monolithic ceramics by the ball-on-disc method. ISO 20808:2016.

Metal cutting tools. Durability testing of turning tools. PN-83/M-58350.

Standard Test Method for Wear Testing with a Pin-on-Disk Apparatus. ASTM G99–95.

Tribology; friction and wear model test for determining the sliding friction of solids (ball-on-disc system). DIN 50324:1992-07.

Technical Sciences, 2019, 22(3), 237–247

UNIWERSYTET WARMIŃSKO-MAZURSKI W OLSZTYNIE

Quarterly peer-reviewed scientific journal
ISSN 1505-4675
e-ISSN 2083-4527
TECHNICAL SCIENCES
Homepage: www.uwm.edu.pl/techsci/

doi: 10.31648/ts.4996

AN ANALYSIS OF NON-ISOTHERMAL PRIMARY CRYSTALLIZATION KINETICS OF $FE_{95}SI_5$ AMORPHOUS ALLOY

Adam Frączyk[1], *Krzysztof Kuś*[2], *Adam Wojtkowiak*[3]

[1]ORCID: 0000-0002-3056-3141
Department of Material and Machine Technology
University of Warmia and Mazury in Olsztyn
[2]ORCID: 0000-0001-9811-5831
Department of Material and Machine Technology
University of Warmia and Mazury in Olsztyn
[3]Department of Material and Machine Technology
University of Warmia and Mazury in Olsztyn

Received 7 October 2019, accepted 26 January 2020, available online 27 January 2020.

Key words: metallic glass, energy activation, Avrami exponent, crystallization kinetics parameter, DSC.

Abstract

The paper describes the primary crystallization of metallic Fe95Si5 glass which was studied by differential scanning calorimetry (DSC) with non-isothermal methods. The activation energy of crystal transformation was calculated with the equations proposed by Kissinger, Mahadevan and a modified version of the equation developed by Augis and Bennett. Activation energy was determined at Ea = 242.0 - 254.2 kJ/mol, subject to the applied method. The Avrami exponent of crystallization in the amorphous phase n was determined in the range of n = 2.40 - 2.52, depending on the method of calculating the transformation of activation energy.

Correspondence: Adam Frączyk, Katedra Technologii Materiałów i Maszyn, Wydział Nauk Technicznych, Uniwersytet Warmińsko-Mazurski, ul. Oczapowskiego 11, 10-719 Olsztyn, phone: +48 89 523 44 43, e-mail: adam.fraczyk@uwm.edu.pl.

Introduction

Amorphous alloys, also known as metallic glass, have numerous industrial applications due to their excellent soft magnetic properties. The properties of amorphous alloys continue to be investigated (LI et al. 2008, SAHINGOZA et al. 2004, NOBUYUKI et al. 2007).

Thermal treatment and nanocrystallization improve the properties of metallic glass. The crystallization of amorphous alloys can be controlled, which is particularly important consideration in the production of materials with a specific structure. These processes require a thorough understanding of the crystallization kinetics of metallic glass.

The crystallization kinetics of chalcogenide glass can be analyzed by isothermal and non-isothermal methods, and the results can be interpreted with the use of several theoretical models (KISSINGER 1957, OZAWA 1970, MATUSITA et al. 1979, MATUSITA et al. 1980, KONG et al. 2011, REZAEI-SHAHREZA et al. 2017). In recent years, new isoconversional methods have been applied to determine the crystallization parameters of amorphous alloys during non-isothermal heating (REZAEI-SHAHREZA et al. 2017, ANSARINIYA et al. 2018, JAAFARI et al. 2018).

Isothermal analyses involve the JMA equation which is a primary method for determining crystallization parameters. However, non-isothermal techniques have also been used in numerous experiments. Different values of crystallization kinetic parameters were reported in Fe-based amorphous alloys. For example, the estimated values of the Avrami exponent ranged from 1.0 to 4.0 (GIBSON et al. 1987, SANTOS et al. 2002). The activation energy of the same alloy can also be calculated with the use of different models and equations. The aim of the present study was to determine the activation energy of the primary crystallization process based on the equations proposed by Kissinger and Mahadevan and the modified version of the equation developed by Augis and Bennett. The Avrami exponent of crystallization kinetics n which describes the mechanism of crystalline phase formation was also calculated.

Theory

The analyses of the crystallization kinetics of amorphous alloys generally involve two parameters: activation energy E_a and the Avrami exponent of crystallization kinetics n.

Both isothermal and non-isothermal methods can be used in calorimetric measurements. Most methods rely on the Johnson-Mehl-Avrami-Kolmogorov (JMAK) equation of isothermal transformation kinetics (MÁLEK 2000, WANG et al. 2014):

$$x(t) = 1 - \exp(-Kt^n) \tag{1}$$

where:

$x(t)$ – volume fraction transformed after time t,
n – the Avrami exponent exponent which reflects the nucleation rate and the growth morphology,
K – the reaction rate constant.

The temperature dependence of the reaction rate is usually determined with the use of the Arrhenius equation:

$$K = K_0 \exp\left(\frac{-E_a}{RT}\right) \tag{2}$$

where:

E_a – the activation energy for the crystallization reaction,
K_0 – the frequency factor,
R – the gas constant.

Non-isothermal crystallization is characterized by a constant heating rate. The relationship between sample temperature T and heating rate β can be expressed by the following equation:

$$T = T_0 + \beta t \tag{3}$$

The activation energy of primary crystallization can be determined using the models developed by Kissinger (KISSINGER 1957), Ozawa (OZAWA 1970), Mahadevan (MAHADEVAN et al. 1986) and Augis-Bennett (AUGIS et al. 1978). These methods are based on the JMAK theory (Eq. 1) and the logarithmic form of Equation 2. These models account for the fact that the volume of the crystallized fraction at the top of the crystallization peak in DSC is x_p=0.63. When the highest rate of transformation is applied at maximum peak approximations, the relevant equations can be interpreted as follows:

a) Kissinger model

$$\ln\left(\frac{\beta}{T_p^2}\right) = \frac{-E_a}{RT_p} + \ln\left(\frac{K_0 R}{E_a}\right) \tag{4}$$

b) Mahadevan model

$$\ln(\beta) = \frac{-E_a}{RT_p} + \ln\left(\frac{K_0 E_a}{R}\right) \tag{5}$$

c) Modified version of the Augis and Bennett model

$$\ln\left(\frac{\beta}{T_p}\right) = \frac{-E_a}{RT_p} + \ln(K_0) \tag{6}$$

where:

T_p – peak temperature,
β=dT/dt – the heating rate.

The partial values of $\ln(K_0R/E_A)$, $\ln(K_0E_A/R)$ and $\ln(K_0)$ in Equations 4, 5 and 6 are constant. From it is possible to derive The value of activation energy E_a and pre-exponential factor K_0 of the crystallization process can be derived from the slope and the intercept of the straight line (Equations 4, 5, 6), respectively.

The Avrami exponent n is also an important crystallization parameter, and it can be determined with the use of various methods. In the model developed by Ozawa, time in Equation 1 was replaced by temperature in Equation 3 to produce the following equation:

$$x(t) = 1 - \exp\left[-\left\{\frac{K(T - T_0)}{\beta}\right\}\right] \tag{7}$$

Double logarithmic transformation can be applied to produce the following equation:

$$\ln[-\ln(1 - x)] = -n\ln(\beta) + n\ln(T - T_0) \tag{8}$$

The values of ln[−ln (1 - x)] are plotted against ln(β) from various DSC thermograms, and the Avrami exponent n is derived from the slope of the straight line (Eq. 8). The Avrami exponent n can also be determined with the following equation (GAO et al. 1986, JAKUBCZYK et al. 2008):

$$n = \left(\frac{\mathrm{d}x}{\mathrm{d}t}\right)_p RT_p^2(0{,}37\beta E_a)^{-1} \tag{9}$$

where:

$(\mathrm{d}x/\mathrm{d}t)_p$ – the maximum crystallization rate.

Experimental

Amorphous samples were obtained by rapid solidification of melts using the melt-spinning method (Fig. 1). The obtained ribbon was 20 mm wide and and 0.03 mm thick. The nominal composition of $Fe_{95}Si_5$ is presented in Figure 2.

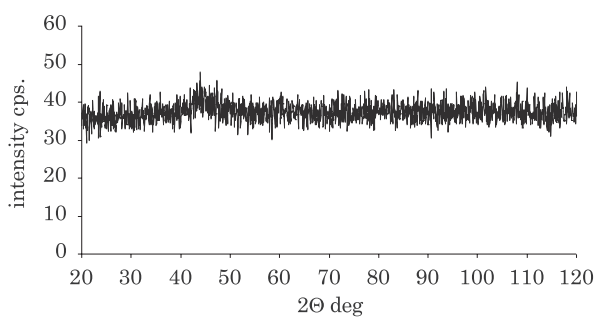

Fig. 1. XRD pattern of $Fe_{95}Si_5$ amorphous alloy

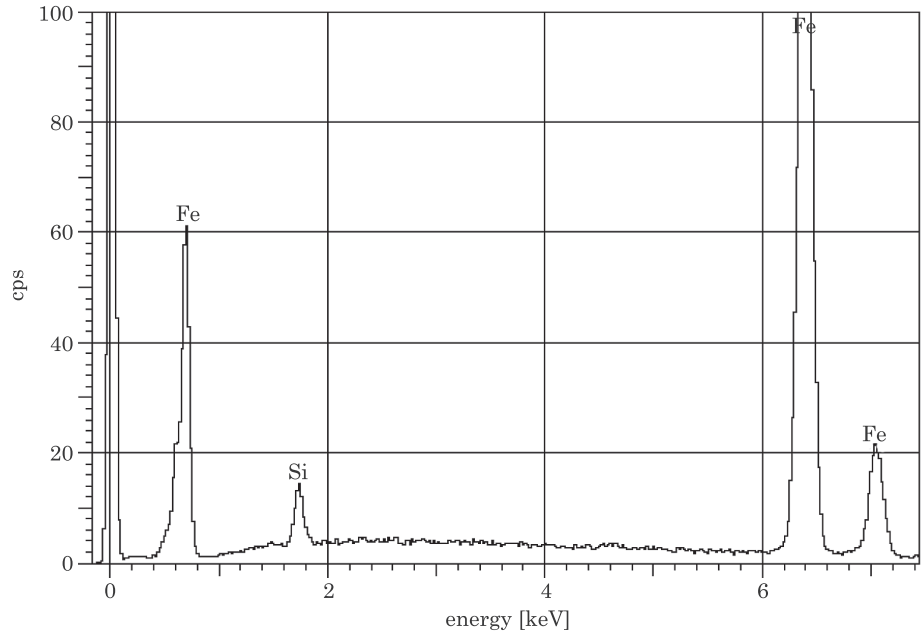

Fig. 2. EDS spectrum of $Fe_{95}Si_5$ amorphous alloy

The crystallization process was investigated by differential scanning calorimetry (DSC) in a nitrogen atmosphere using the Netzsch DSC 204 differential scanning calorimeter. Temperature and energy calibrations were performed based on the melting temperatures and melting enthalpies of high-purity zinc and indium registered in the device. Sample mass in DSC measurements approximated several milligrams. The samples were heated from 340 K to 840 K at different heating rates (β = 5, 10, 20 and 30 K min^{-1}).

Results and Discussion

The DSC thermograms for the crystallization of $Fe_{95}Si_5$ at various heating rates are presented in Figure 3. The two crystallization peaks of $Fe_{95}Si_5$ involve two resolved phase transformations. The position of both peaks shifted to higher temperatures with an increase in heating rate. The first peak corresponds to phase formation in α-Fe(Si) (FRĄCZYK 2011). The observed shift of the onset of crystallization T_x to higher temperatures is the result of the induction time of the nucleation process. There is a nucleation time during crystallization. When the heating rate increases, the onset of crystallization shifts to higher temperatures.

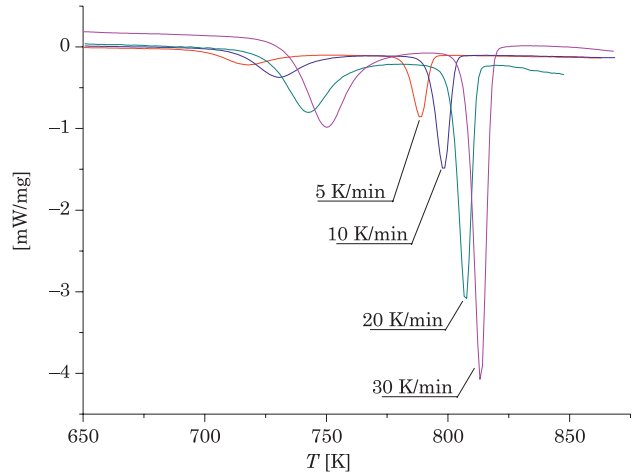

Fig. 3. DSC curves of $Fe_{95}Si_5$ for several heating rates illustrating primary crystallization (first peak) and secondary crystallization (second peak) processes

The activation energy E_a of the primary crystallization of $Fe_{95}Si_5$ metallic glass was calculated with the use of the models proposed by Kissinger and Mahadevan and the modified version of the Augis and Bennett model (4-6). For this purpose, the values of $\ln(\beta/T_p^2)$ vs. $10^3/T_p$ (Fig. 4), $\ln(\beta)$ vs. $10^3/T_p$ (Fig. 5) and $\ln(\beta/T_p^2)$ vs. $10^3/T_p$ (Fig. 6) were plotted for the amorphous alloy.

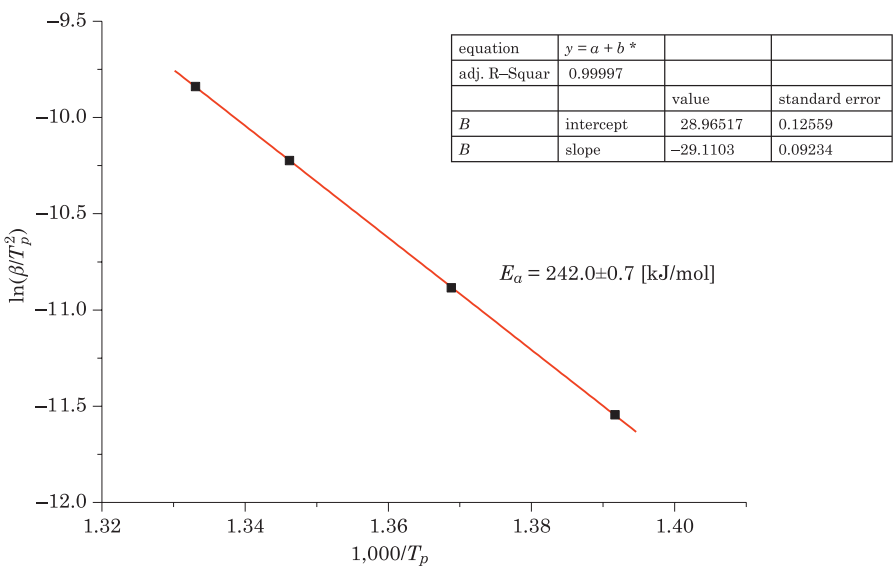

equation	y = a + b *		
adj. R–Squar	0.99997		
		value	standard error
B	intercept	28.96517	0.12559
B	slope	–29.1103	0.09234

Fig. 4. Plot of $\ln(\beta/T_p^2)$ vs 1,000/Tp values for the determination of activation energy E_a from a set of DSC scans with different heating rates (5, 10, 20 and 30 K/min). The analysis was performed for the first exothermic DSC reaction of $Fe_{95}Si_5$ amorphous alloy

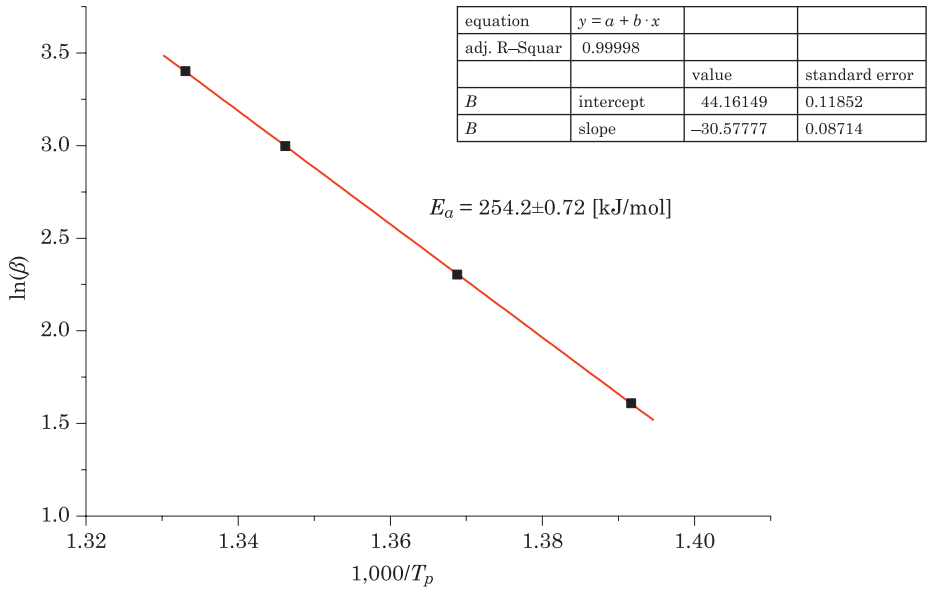

Fig. 5. Plot of ln(β) vs 1,000/Tp values for the determination of activation energy E_a from a set of DSC scans with different heating rates (5, 10, 20 and 30 K/min). The analysis was performed for the first exothermic DSC reaction of $Fe_{95}Si_5$ amorphous alloy

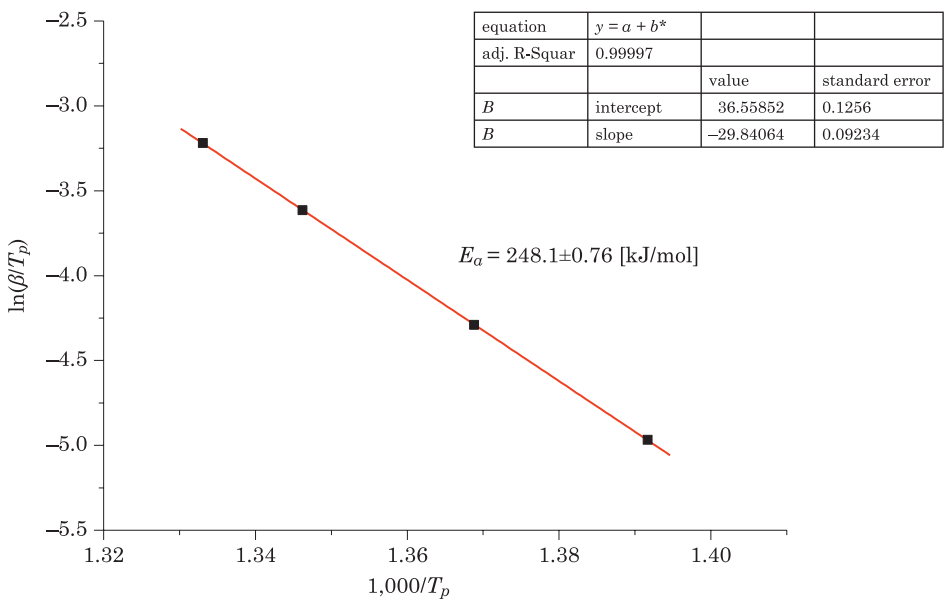

Fig. 6. Plot of ln(β/T_p) vs 1,000/T_p values for the determination of activation energy E_a from a set of DSC scans with different heating rates (5, 10, 20 and 30 K/min). The analysis was performed for the first exothermic DSC reaction of $Fe_{95}Si_5$ amorphous alloy

The activation energy E_a of an amorphous alloy can be derived from the slope ($-E_a/R$) of the line. The line of best fit was determined with the least squares method. The arithmetic mean and standard deviation were calculated for activation energies. The results are presented in Table 1.

Table 1

Parameters of primary crystallization kinetics of $Fe_{95}Si_5$ metallic glass

Parameter	Kissinger equation	Mahadevan equation	Modified version of the Augis & Bennett equation
Ea [kJ/mol]	242.0	254.2	248.1
N	2.52	2.46	2.40

The crystallized fraction x at temperature T was expressed as $x(T) = Ax(T)/A$, where A and Ax represent the total area and the partial area (at generic temperature T) of the exothermic peak, respectively. The relationship between the crystallized volume fraction and the time of the first exothermic peak of amorphous $Fe_{95}Si_5$ alloy is presented in Figure 7.

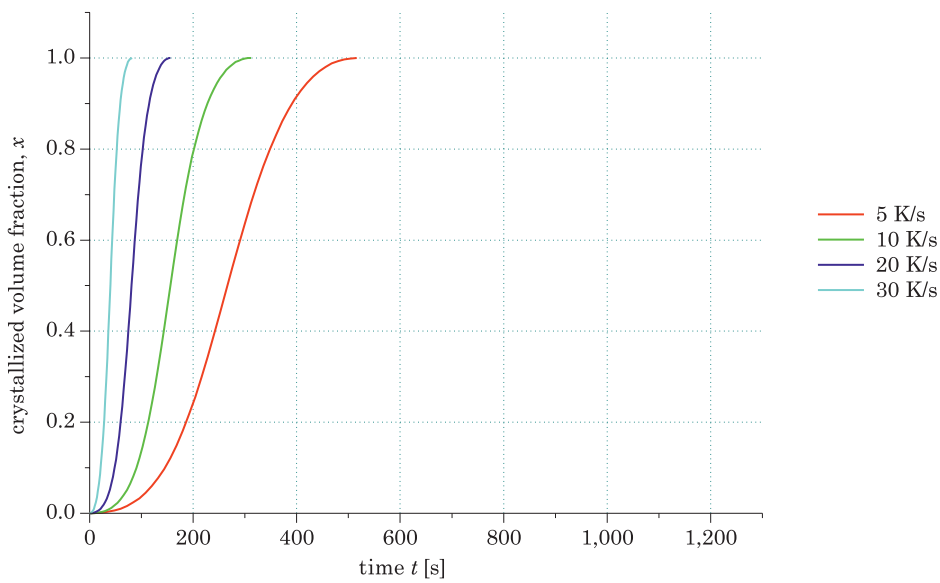

Fig. 7. Crystallized volume fraction $\boldsymbol{x}$ as a function of time $\boldsymbol{t}$ for $Fe_{95}Si_5$ metallic glass at different heating rates β

In Figure 8, the data from Figure 5 were expressed as a function of time t to illustrate the relationship between crystallization rate dx/dt and temperature T.

The Avrami exponent n was calculated by substituting the maximum value of dx/dt into Equation 9 for different heating rates. The primary crystallization parameters are presented in Table 1.

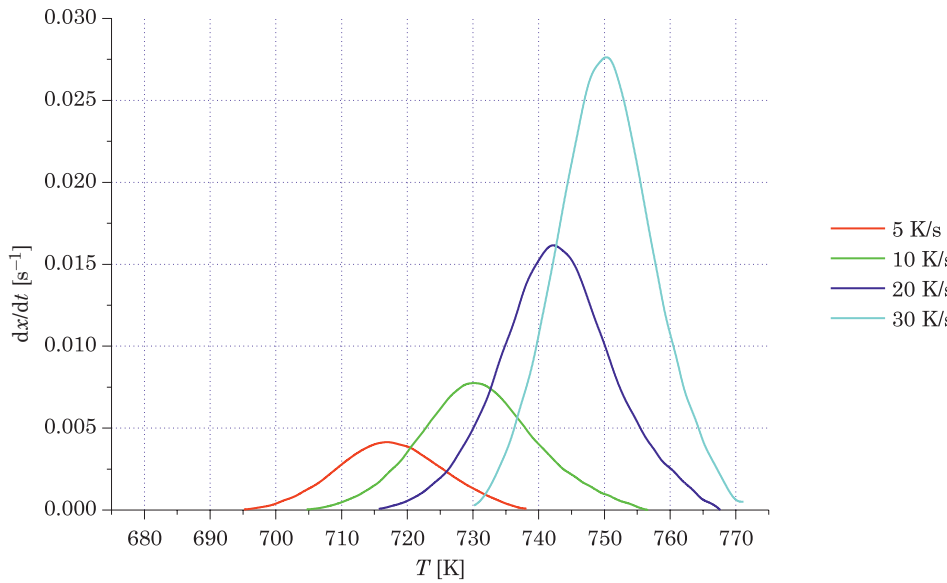

Fig. 8. Curve of crystallization rate dx/dt vs temperature T for $Fe_{95}Si_5$ amorphous alloy at different heating rates β

Activation energy E_a and the Avrami exponent n are the most important kinetic parameters describing the crystallization of amorphous alloys. The highest activation energy E_a was obtained with the Mahadevan equation (Equation 5), and the lowest activation energy was obtained with the Kissinger equation (Equation 4). The extreme values of E_a differed by nearly 5%.

Similar results were reported by AL-HENITI (2009) in an analysis of the crystallization kinetics of $Fe_{78}Ni_{1.5}Si_9B1_3$ metallic glass.

Conclusions

The values of activation energy and the Avrami exponent n, which are associated with the first peak temperature in continuous heating DSC curves of amorphous $Fe_{95}Si_5$ alloy, were estimated with the use of acclaimed methods.

The values of Avrami exponent n indicate that during the first stages of the crystallization process a crystal growth controlled respectively by diffusion and by interface takes place.

In order compare the activation energy of different amorphous alloys the same equation or model should be applied.

References

AL-HENITI S.H. 2009. *Kinetic study of non-isothermal crystallization in $Fe_{78}Si_9B_{13}$ metallic glass*. Journal of Alloys and Compounds, 484: 177–184.

ANSARINIYA M., SEIFODDINI A., HASANI S. 2018. *$(Fe_{0.9}Ni_{0.1})_{77}Mo_5P_9C_{7.5}B_{1.5}$ bulk metallic glass matrix composite produced by partial crystallization: The non-isothermal kinetic analysis*. Journal of Alloys and Compounds, 763: 606–612.

AUGIS J.A., BENNTT J.E. 1978. *Calculation of the Avrami Parameters for Heterogeneous Solid State Reactions Using a Modification of the Kissinger Method*. Journal of Thermal Analysis, 13: 283–292.

FRĄCZYK A. 2011. *The activation energy of primary crystallization of $Fe_{95}Si_5$ metallic glass*. Technical Science, 14(1): 93-100.

GAO Y.Q., WANG W. 1986. *On the activation energy of crystallization in metallic glasses*. Journal of Non-Crystalline Solids, 81: 129–134.

GIBSON M.A., DELAMORE G.W. 1987. *Crystallization kinetics of some iron-based metallic glasses*. Journal of Material Science, 22(12): 4550–4557.

JAKUBCZYK E., KRAJCZYK A., JAKUBCZYK M. 2008. *Crystallization of amorphous $Fe_{78}Si_9B_{13}$ alloy*. Journal of Physics: Conference Series, 79: 012008.

JUNG H. Y., STOICA M., YI S., KIM D.H., ECKERT J. 2015. *Crystallization Kinetics of $Fe_{76.5-x}C_{6.0}Si_{3.3}B_{5.5}P_{8.7}Cu_x$ (x = 0, 0.5, and 1 at. pct) Bulk Amorphous Alloy*. Metallurgical and Materials Transactions, 46(A): 2415-2421.

JAAFARI Z., SEIFODDINI A., HASANI S., REZAEI-SHAHREZA P. 2018. *Kinetic analysis of crystallization process in $[(Fe_{0.9}Ni_{0.1})_{77}Mo_5P_9C_{7.5}B_{1.5}]_{100-x}Cu_x$ (x = 0.1 at.%) BMG*. Journal of Thermal Analysis and Calorimetry, 134: 1565–1574.

KISSINGER H. E. 1957. *Reaction kinetics in differential thermal analysis*. Analytical Chemistry, 29: 1702–1706.

KONG L.H., GAO Y.L., SONG T.T., WANG G., ZHAI Q. J. 2011. *Non-isothermal crystallization kinetics of FeZrB amorphous alloy*. Thermochimica Acta, 522: 166–172.

LI H.X., JUNG H.Y., YI S. 2008. *Glass forming ability and magnetic properties of bulk metallic glasses $Fe_{68.7-x}C_{7.0}Si_{3.3}B_{5.5}P_{8.7}Cr_{2.3}Mo_{2.5}Al_{2.0}Co_x$ (x = 0–10)*. Journal of Magnetism and Magnetic Materials, 320: 241–245.

MAHADEVAN S., GIRIDHAR A., SINGH A.K. 1986. *Calorimetric measurements on as-sb-se glasses*. Journal of Non-Crystalline Solids, 88(1): 11–34.

MÁLEK J. 2000. *Kinetic analysis of crystallization processes in amorphous materials*. Thermochimica Acta, 355: 239–253.

MATUSITA K, SAKKA S. 1979. *Kinetic Study of the Crystallisation of Glass by Differential Scanning Calorimetry*. Physics and Chemistry of Glasses, 20: 81–84.

MATUSITA K, SAKKA S. 1980. *Kinetic study of crystallization of glass by differential thermal analysis-criterion on application of Kissinger plot*. Journal of Non-Crystalline Solids, 38–39(2): 741–746.

NOBUYUKI N., KENJI A., AKIHISA I. 2007. *Novel applications of bulk metallic glass for industrial products*. Journal of Non-Crystalline Solids, 353: 3615-3621.

OZAWA T. 1970. *Kinetic analysis of derivative curves in thermal analysis*. Journal of Thermal Analysis, 2: 301–324.

REZAEI-SHAHREZA P., SEIFODDINI A., HASANI S. 2017. *Thermal stability and crystallization process in a Fe-based bulk amorphous alloy: The kinetic analysis*. Journal of Non-Crystalline Solids, 471: 286–294.

REZAEI-SHAHREZA P., SEIFODDINI A., HASANI S. 2017. *Non-isothermal kinetic analysis of nano-crystallization process in $(Fe_{41}Co_7Cr_{15}Mo_{14}Y_2C_{15})_{94}B_6$ amorphous alloy*. Thermochimica Acta, 652: 119–125.

SAHINGOZA R., EROLA M., GIBBS M.R.J. 2004. *Observation of changing of magnetic properties and microstructure of metallic glass $Fe_{78}Si_9B_{13}$ with annealing*. Journal of Magnetism and Magnetic Materials, 271: 74–78.

SANTOS D.S., SANTOS D.R., BIASI R.S. 2002. *Study of crystallization in the Fe86Cu1Zr7B6 amorphous alloy using FMR and DSC*. Journal of Magnetism and Magnetic Materials, 242–245(2): 882–884.

WANG T., YANG X., LI Q. 2014. *Effect of Cu and Nb additions on crystallization kinetics of $Fe_{80}P_{13}C_7$ bulk metallic glasses*. Thermochimica Acta, 579: 9–14.

Technical Sciences, 2019, 22(3), 249–262

UNIWERSYTET WARMIŃSKO-MAZURSKI W OLSZTYNIE

Quarterly peer-reviewed scientific journal
ISSN 1505-4675
e-ISSN 2083-4527
TECHNICAL SCIENCES
Homepage: www.uwm.edu.pl/techsci/

doi: 10.31648/ts.5001

INFLUENCE OF GAS DETONATION SPRAYING PARAMETERS ON THE GEOMETRICAL STRUCTURE OF FE-AL INTERMETALLIC PROTECTIVE COATINGS*

***Tomasz Chrostek*[1], *Mirosław Bramowicz*[2], *Kazimierz Rychlik*[3], *Adam Wojtkowiak*[4], *Cezary Senderowski*[5]**

[1]ORCID: 0000-0002-6516-8192
Department of Materials and Machine Technology
University of Warmia and Mazury in Olsztyn
[2]ORCID: 0000-0002-7716-544X
Department of Materials and Machine Technology
University of Warmia and Mazury in Olsztyn
[3]ORCID: 0000-0003-2978-4681
Research Network ŁUKASIEWICZ
Institute of Mechanized Construction and Rock Mining, Warsaw
[4]Department of Materials and Machine Technology
University of Warmia and Mazury in Olsztyn
[5]ORCID: 0000-0002-0331-3702
Department of Materials and Machine Technology
University of Warmia and Mazury in Olsztyn

University of Warmia and Mazury in Olsztyn Received 7 October 2019,
accepted 29 January 2020, available online 31 January 2020.

K e y w o r d s : GDS, Detonation Gas Spraying, Fe-Al, intermetallic alloys, fractal analysis, RMS.

A b s t r a c t

The paper presents the results of an analysis of the geometrical structure of Fe-Al intermetallic protective coatings sprayed under specified gun detonation spraying (GDS) conditions. Two barrel lengths, two powder injection positions (PIP) at the moment of spark detonation, and two numbers of GDS shots with 6.66 Hz frequency were applied as variable parameters in the GDS process.

Correspondence: Tomasz Chrostek, Katedra Technologii Materiałów i Maszyn, Wydział Nauk Technicznych, Uniwersytet Warmińsko-Mazurski, ul. Oczapowskiego 11/E27, 10-719 Olsztyn, phone: +48 89 5233855, e-mail: tomasz.chrostek@uwm.edu.pl.

* This study was financed as part of project No. 2015/19 / B / ST8 / 02000 of the Polish National Science Center of Poland.

Surface profile measurements were conducted by contact profilometry with the use of the TOPO-01 system and the Mitutoyo SJ 210 profilometer. The measured parameters were used to analyze surface topography in two-dimensional (2D) and three-dimensional (3D) systems. It was assumed that roughness can be regarded as a non-stationary parameter of variance in surface amplitude which is highly dependent on the sampling rate and spraying distance. Therefore, changes in surface amplitude parameters and functional properties were analyzed across segments with a length (*ln*) of 1.25, 4 and 12.5 mm. The development of the geometric structure of the surface was analyzed with the RMS (Root Mean Square) fractal method, and the geometric structure of the surface stretched by several orders of magnitude was evaluated based on the correlation between roughness (*Rq*), segment length (*ln*) and fractal dimension (*D*). The RMS method and the calculated fractal dimension (*D*) supported the characterization of the geometric structure of intermetallic Fe-Al protective coatings subjected to GDS under the specified process conditions based on the roughness profiles of surface segments with a different length (*ln*).

Introduction

Intermetallic alloys based on ordered intermetallic phases belong to a group of innovative engineering materials used in industry. This group includes alloys from the Fe-Al equilibrium system which are functional materials with unique performance properties that can be applied as protective coatings in high-temperature environments (BYSTRZYCKI et al. 1996). Intermetallic alloys are particularly suited for use as heat-resistant construction materials on account of their resistance to high temperature corrosion in aggressive sulfide and chloride environments. However, high brittleness and the problems associated with the production of solid alloys with a fine-grained structure that are free of structural defects (JASIONOWSKI et al. 2011, 2012, NIEWIELKI, JABŁOŃSKA 2007) pose a major limitation to the widespread use of intermetallic alloys.

Despite their weaknesses, Fe-Al intermetallic alloys have a number of important functional properties, including excellent oxidation resistance, structural and chemical stability at elevated temperatures and, equally importantly, the ability to form Al_2O_3 oxides on the surface. A tight protective oxide layer increases resistance to oxidation, carburization and sulfation, which renders iron-aluminum intermetallics suitable for the production of components that operate in an aggressive gas environment. The above was confirmed by studies where Fe-Al intermetallic alloys with 28-Fe at% Al and 35-Fe at% Al were significantly more resistant to heat than the components made of commercial chromium-nickel steel (Fe-25Cr-20Ni) and chromium-aluminum (19-Fe at% and 12-Cr at% Al). FeAl alloys are used in aluminum extrusion and in the production of grate bars that are resistant to furnace operations at roughly 1,000°C. They are also applied in the production of intermetallic (FeAl) pallets and stands in both heat and chemical treatment furnaces, furnace rails and rollers for transporting hot-rolled steel sheets (BYSTRZYCKI et al. 1996, JASIONOWSKI et al. 2011, NIEWIELKI, JABŁOŃSKA 2007, SCHNEIBEL et al. 2005). Intermetallic

alloys are also relatively cheaper than other groups of heat-resistant materials (JASIONOWSKI et al. 2011, NIEWIELKI, JABŁOŃSKA 2007).

Conventional methods of producing Fe-Al intermetals, such as melting or casting, can be problematic. Therefore, thermal spraying methods that produce coatings with potentially promising properties and are characterized by adhesive bonding to the base material are becoming increasingly popular. Several thermal spraying methods produce coatings with different properties and applications, depending on the type of spraying equipment and process parameters. Many years of research and industrial experience have led to the development of technologies that differ in the generation and acceleration of the metallizing stream containing particles of the coating material. Coatings are generally produced with the involvement of the available spray metallization methods, including (ASSADI 2016, CINCA, GUILEMANY 2012, CHEN et al. 2009, HEJWOWSKI 2013, MUŠALEK et al. 2010, SENDEROWSKI et al. 2011, SENDEROWSKI 2015, SZULC 2013, XU et al. 2004, YAN et al. 2012, ŻÓRAWSKI 2010):

a) High Velocity Arc Spraying (HVAS),
b) Atmospheric Plasma Spraying (APS),
c) High Velocity Oxygen Fuel (HVOF),
d) Cold Spraying,
e) Gas Detonation Spraying (GDS).

Thermal spraying technologies are usually quite complex processes whose parameters affect coating performance regardless of the applied method. All thermal spraying methods are characterized by specific temperature and velocity of the metallizing stream which determine the kinetic energy of powder charge particles that form the coating. These methods support the production of coatings with the required properties, such as porosity, hardness, adhesive strength, natural stress distribution and oxidation state, within a short period of time (BOJAR et al. 1996).

Gun detonation spraying (GDS) is a popular coating method, but the technological requirements during the supersonic flow of a two-phase (gas-powder) metallization stream and the formation of a layered coating structure with oxide phases formed in-situ during GDS are still in the research phase (SENDEROWSKI et al. 2011).

The GDS process produces geometrically uniform coatings with an axially symmetric thickness distribution. This effect can be achieved by monitoring the entire spraying process and its repeatability in each working cycle. Coating geometry is generally determined by the speed with which powder particles collide with the base material and the thermal energy released during this event (SENDEROWSKI et al. 2011). The aim of this study was to determine the effect of the length of the GDS gun barrel on the geometry, performance, functional properties, including roughness, and fractal properties of coatings.

Materials and Methods

Four coatings produced by gun detonation spraying of intermetallic powder material based on the FeAl phase matrix with 40% aluminum content were tested. The powder with 5-40 μm particle size was manufactured by the Vacuum Inert Gas Atomization (VIGA) method. The substrate was 15 HM boiler steel measuring 50×50×5 mm (Fig. 1). The surface layer of the substrate material was blasted with alumina before spraying. Circular coatings were obtained by placing the substrate material in a stationary position relative to the barrel outlet.

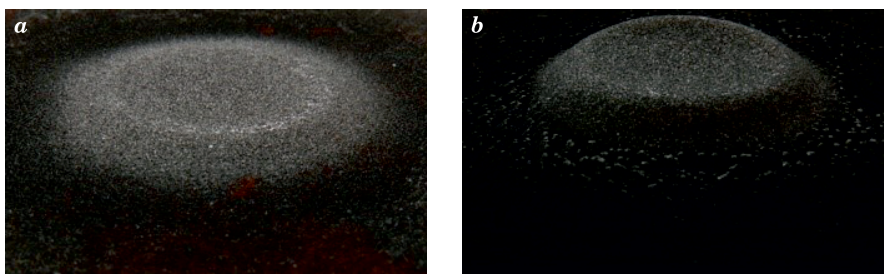

Fig. 1. FeAl coatings sprayed onto 15 HM boiler steel by the GDS method with: *a* – 100, *b* – 400 shots, without changing the position of the barrel relative to the base material

Intermetallic materials based on the FeAl phase are characterized by considerable resistance to high temperatures in chemically aggressive environments, stable and ordered structure up to around 1,100°C, and significant resistance to both abrasive and erosive tribological wear (CHROSTEK et al. 2018). The GDS process was carried at the Paton Institute in Kiev with the use of the Perun-S gun with different spraying parameters (Tab. 1).

Table 1

GDS parameters

Fe40Al0.05Zr at% powder +50 ppm *B*			Granulation 5–40 μm		
Oxygen-fuel mixture			C_3H_8 – 0.45 m^3/h O_2 – 1.52 m^3/h air – 0.65 m^3/h		
Air flow rate			0.4 m^3/h		
Spraying frequency			f = 6.66 Hz		
Coating	spraying distance *L* [mm]	barrel length [mm]	PIP* [mm]	number of GDS shots	coating thickness [mm]
1	110	590	412.5	400	2.91
2			274.5	100	0.86
3		1,090	412.5	100	0.56
4			274.5	400	1.13

* powder injection position – location of powder in the barrel at the time of detonation

Different powder injection positions (PIP), i.e. powder locations in the barrel at the moment of ignition initiation, a different number of shots, and different barrel lengths were applied during the experiment. Coatings were formed through cyclical gradient concentration deposition at a frequency of 6.66 Hz, with a constant composition of the explosive mixture (propane) as the working gas. The distance between the barrel (Ø23 mm inner diameter) and the sprayed substrate was L = 110 mm.

Surface profilometric measurements were carried out by the contact method with the TOPO-01 modular measuring system which measures shape contours on flat cylindrical external and internal surfaces. The system's high accuracy and broad measuring range support a comprehensive characterization of the surface profile based on 2D measurements of roughness, wave and shape. Stereometric 3D measurements can be performed by moving the analyzed object in the Y-axis on a table. The measuring head has a diamond tip with a 2 μm radius and a 60° cone angle (Fig. 2).

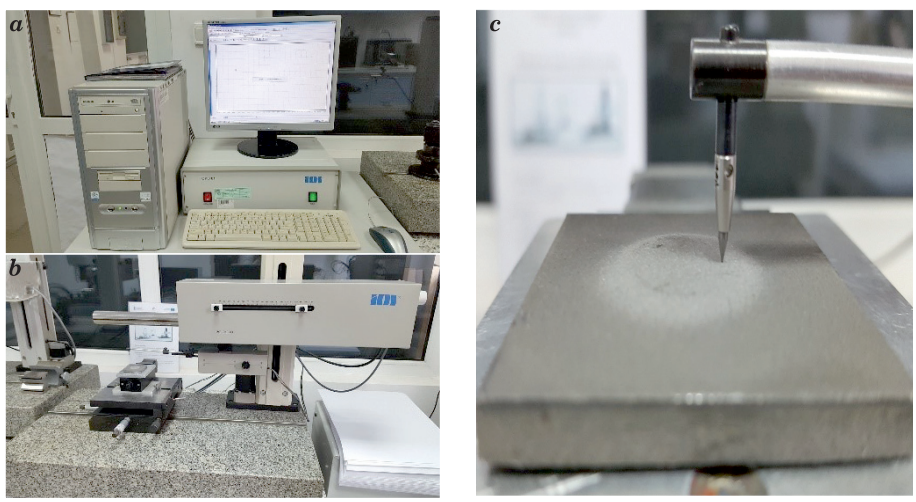

Fig. 2. TOPO-01 system for measuring surface topography: *a* – computer with the TOPO-01 control module, *b* – PG 2/200 shape-maker for 3D stereometric measurements, *c* – measuring head

Coating surfaces were analyzed in 26 passes at a speed of 1 mm/s in increments of 1 mm. The measured area was 25×25 mm. The measured parameters are given in Table 2.

Surface roughness tests were carried out using the Mitutoyo SJ-210 contact device. The measuring head has a cone-shaped diamond blade with an angle of 60° and a tip radius of 2 μm. The surface mapping range is 360 μm (from -200 to +160 μm).

Table 2

Coating surface topography

X-axis feed	25 mm
Y-axis feed	25 mm
Feed speed	1 mm/s
Number of passes	26
Stroke in the Y-axis	every 1 mm
Straightness	0.3 μm/25 mm
Resolution	0.1 μm
Maximum head load (auto)	15 N

Roughness was regarded a non-stationary parameter of variance in surface amplitude which is determined by sampling density and the length of the measuring segment. Changes in amplitude and the functional properties of the tested surface were analyzed across segments with a length (ln) of 1.25, 4 and 12.5 mm.

Roughness parameters denote the statistical distribution of points across the analyzed segment of the tested surface (SAYLES, THOMAS 1978). According to the cited authors, surface height variance (σ^2) is proportional to sampling length, which is described by the below relationship (1):

$$\sigma^2 \propto L \tag{1}$$

The following relationship (2) was proposed by BERRY and HANNAY (1978) to describe variance as a function of scale:

$$\sigma^2 \propto L^H \tag{2}$$

For this reason, the root mean square (RMS) method (BHUSHAN 1999, MAINSAH et al. 2001, AUE 1997) was applied in this study. The RMS approach is a fractal method that provides information about the degree of surface development. It is used to describe the geometric structure of a surface stretched by several orders of magnitude. In this experiment, the fractal dimension (D) was calculated to describe the surface profile across the measured segment with a length (ln) of 1.25 to 12.5 mm. In two-dimensional systems such as surface profiles, D ranges from 1 to 2, where $D = 1$ denotes a straight line, and $D = 2$ denotes an extremely developed surface that consists of an infinite number of sections. Equation (2) takes on the following form (3) when it is applied to roughness Rq based on the relationship between the fractal dimension and the Hurst parameter (H):

$$Rq \propto L^{\frac{2-D}{2}} \tag{3}$$

Three basic waveforms are obtained by plotting the relationship (3) in a logarithmic system (Fig. 3).

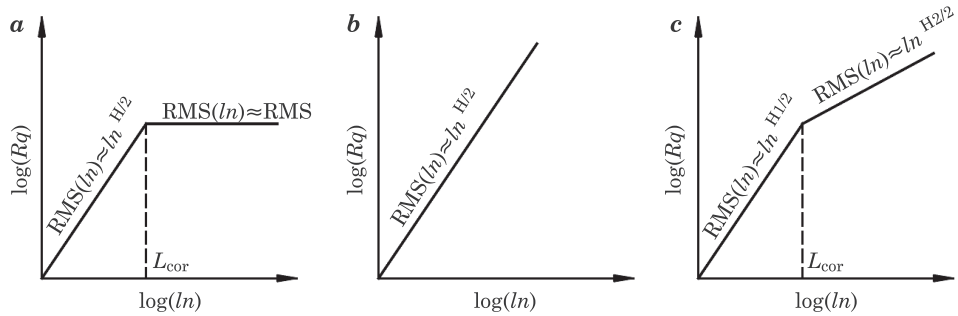

Fig. 3. Basic relationships of $Rq = f(L)$

Source: based on AUE (1997).

In Figure 3*a*, the surface topography of the measured segment with length $< L_{cor}$ is governed by scaling laws. When the above length is exceeded, roughness becomes a stationary process, and Rq is no longer determined by the length of the measured segment. Such surfaces can be described by the fractal dimension D in the range of $L < L_{cor}$, where the value of D is related to the exponent: $\frac{H}{2} = 2 - D$. The surface presented in Figure 3*b* exhibits fractal properties across the entire range of the measurements, whereas the surface in Figure 3*c* has

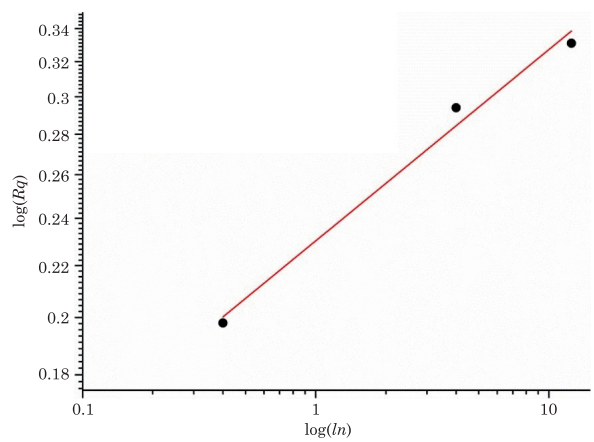

equation	$y = a + b \cdot x$		
weight	no weighting		
residual sum of squares	3.22079E-4		
pearson's r	0.99409		
adj. R-Square	0.97641		
		value	standard error
B	intercept	–0.63787	0.01263
	slope	0.15254	0.01666

Fig. 4. The application of the RMS method in profilometric measurements

bifractal properties. These type of structures correspond to cluster structures, where cluster surface is characterized up to the length L_{cor}, and the structure of cluster arrangement is characterized for $L > L_{cor}$.

In this study, the RMS method was used in profilometric measurements. Points with coordinates (ln, Rq) were plotted in the log-log system, and point relationships were approximated by the power function $y = ax^b$ whose logarithmic form is a linear function with a directional coefficient $1 - \frac{D}{2}$. An exemplary $\log(Rq) = f(\log(ln))$ relationship is shown in Figure 4.

The RMS method supported the description of spray-coated surfaces across the measured sections with a length of 1.25 to 12.5 mm and provided information about surface development.

Results and Discussion

The results of the performed analyses were used to generate isometric views and contour maps describing the analyzed surface and the parameters characterizing the three-dimensional surface of the coatings. Geometrically homogeneous coatings with an estimated diameter of 25 mm, whose thickness was determined by the applied spraying parameters, were formed by 100 and 400 cyclically fired shots with fixed barrel position relative to the sprayed substrate. An analysis of the obtained profilographs indicates that spraying parameters significantly influenced the shape, flat dimensions and thickness distribution of the sprayed coatings (Fig. 5). Regardless of the number of fired GDS shots,

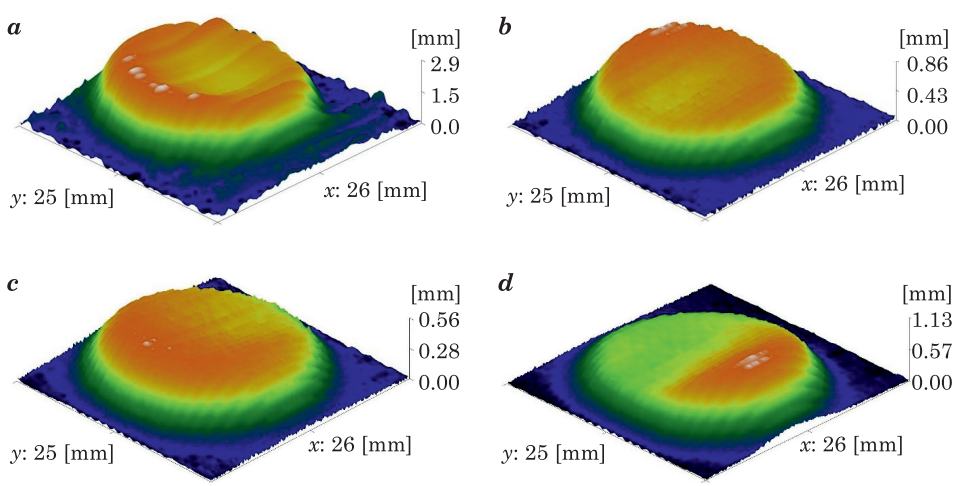

Fig. 5. Isometric view of Fe-Al coatings after GDS spraying – coating numbers correspond to the data in Table 1: a – 1, b – 2, c – 3, d – 4

barrel length exerted the greatest impact on coating thickness. The coatings produced with the use of a shorter barrel (590 mm) were much thicker than those formed with a longer barrel (1,090 mm).

Depending on the applied spraying parameters, the maximum thickness zone of a "static" coating is geometrically shifted by around 6 to 8 mm relative to the barrel axis (Fig. 6). The axially asymmetric distribution of coating thickness indicates that:

– the stream of detonation products entered into dynamic interactions with the substrate and powder particles transported by the stream,

– powder particles were unevenly distributed in the stream of detonation products, which lead to uneven heating of particles at different flow rates,

– more dispersed powder particles (shifted from the axis of the detonation stream) are less deformed after colliding with the substrate.

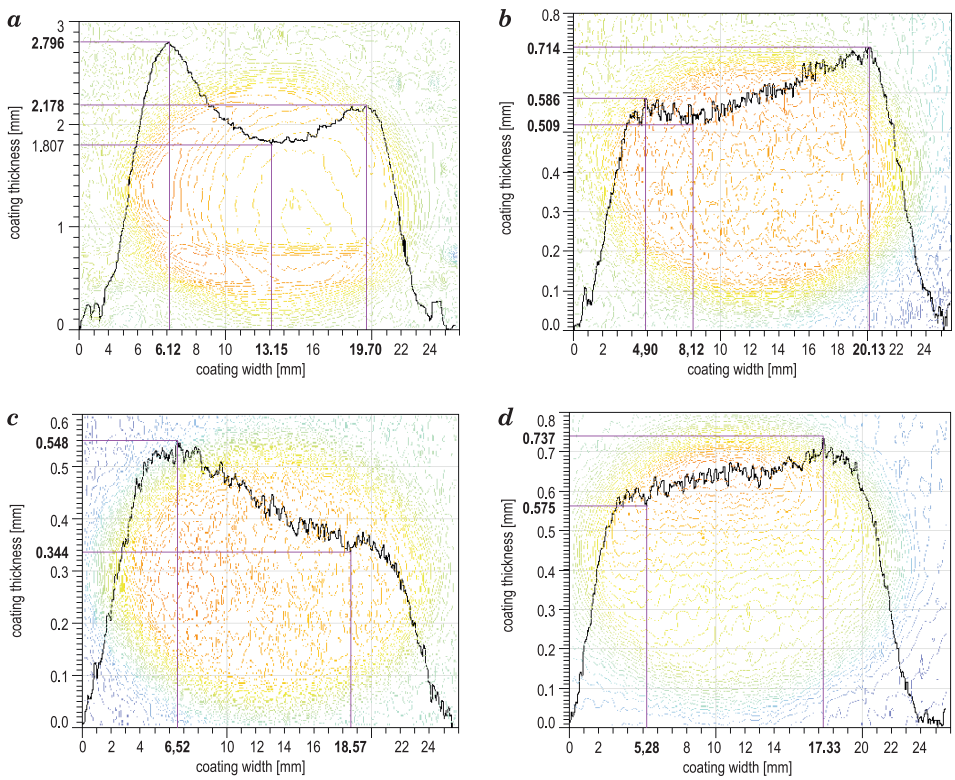

Fig. 6. Thickness distribution of Fe-Al coatings across the cross-sectional diameter and contour maps – coating numbers correspond to the data in Table 1: *a* – 1, *b* – 2, *c* – 3, *d* – 4

a

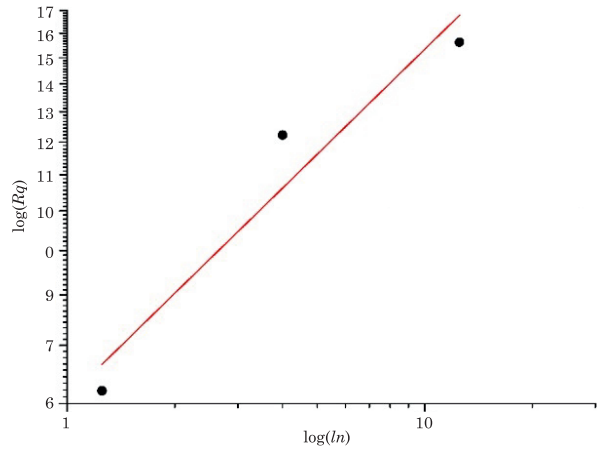

equation	$y = a + b \cdot x$		
weight	no weighting		
residual sum of squares	0.00561		
pearson's r	0.9669		
adj. R-Square	0.8698		
		value	standard error
B	intercept	0.7842	0.07678
	slope	0.4016	0.10596

b

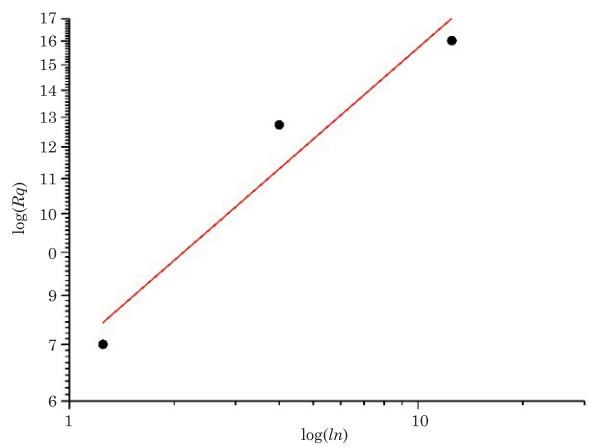

equation	$y = a + b \cdot x$		
weight	no weighting		
residual sum of squares	0.00403		
pearson's r	0.96988		
adj. R-Square	0.88134		
		value	standard error
B	intercept	0.8362	0.06548
	slope	0.3598	0.09037

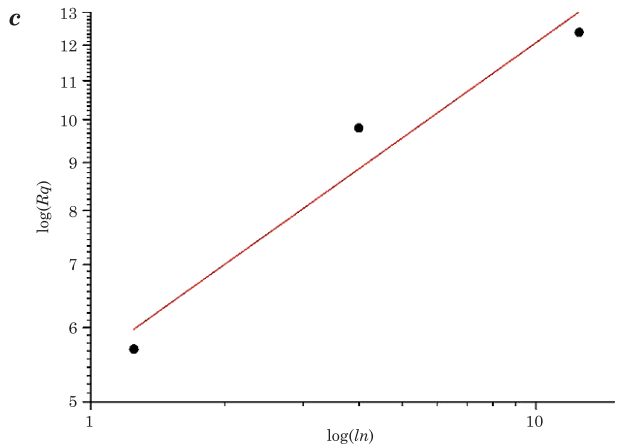

equation	$y = a + b \cdot x$		
weight	no weighting		
residual sum of squares	0.00283		
pearson's r	0.9761		
adj. R-Square	0.9056		
		value	standard error
	intercept	0.7437	0.05455
B	slope	0.3382	0.07528

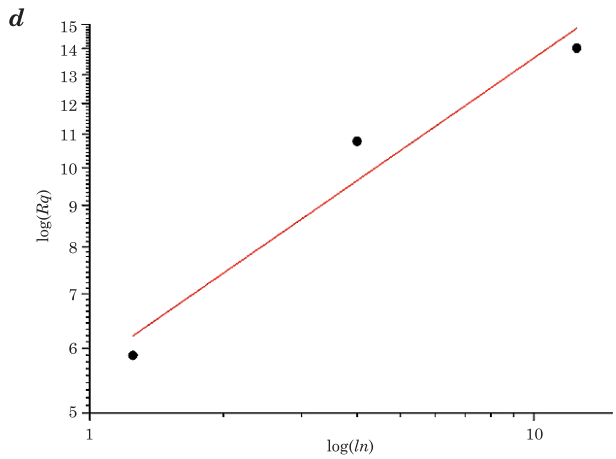

equation	$y = a + b \cdot x$		
weight	no weighting		
residual sum of squares	0.00348		
pearson's r	0.9764		
adj. R-Square	0.9069		
		value	standard error
	intercept	0.7570	0.06043
B	slope	0.3776	0.0834

Fig. 7. Root mean square deviation (RMS) of roughness as a function of the length of the scanned area (*ln*) – coating numbers correspond to the data in Table 1: *a* – 1, *b* – 2, *c* – 3, *d* – 4

Surface roughness is a non-stationary process, and roughness parameters indicate the extent to which roughness is influenced by sampling density and the length of the measured segment. The formed coatings had irregular shape; therefore, roughness was measured in the center. The root mean square deviation of roughness as a function of the scanned area, plotted in a logarithmic coordinate system, is presented in Figure 7. Roughness parameters denote the static distribution of points on the tested surfaces. An analysis of the obtained results revealed that the number of GDS shots exerted the greatest influence on the degree of surface development. The degree of surface development decreased with a rise in the number of GDS shots (Tab. 3).

Table 3

RMS test results

Coating	Length *Ln* [mm] of the scanned segment	Root mean square deviation *Rq* [um]	Slope *a*	Fractal dimension *D*
1[a]	1.25	6.2072	0.4016	1.1968
	4	12.2248		
	12.5	15.6286		
2[b]	1.25	7.0036	0.3598	1.2804
	4	12.7372		
	12.5	16.0178		
3[b]	1.25	5.6892	0.3382	1.3236
	4	9.7922		
	12.5	12.3834		
4[a]	1.25	5.8858	0.3776	1.2448
	4	10.7782		
	12.5	14.0264		

[a] Coating 1 and 4 – 400 GDS shots fired
[b] Coating 2 and 3 – 100 GDS shots fired

Conclusions

The described experiment supported the characterization of the geometric structure of the surface of FeAl-type intermetallic protective coatings formed by gun detonation spraying. The study demonstrated that barrel length significantly affected coating thickness. Regardless of the number of fired GDS shots, the thickest coatings were formed when barrel length was 590 mm.

The RMS method can be used to confirm fractal surface properties. Coating surfaces are governed by scaling laws and are statistically self-similar (each segment of the profile on a given scale is similar to the whole) within the measured

range of 1.25 to 12.5 mm. The degree of surface development decreased with a rise in the number of fired shots. The above can probably be attributed to shock-wave compaction effects during cyclic operation of the GDS gun, which acts a precursor of gaseous detonation combustion products that transport powder particles of FeAl coating.

References

ASSADI H., KREYE H., GARTNER F., KLASSEN T. 2016. *Cold spraying – A materials perspective*. Acta Materialia, 116: 382-407.

AUE J.-J. 1997. *Fractals and fracture: structure-property relationship of highly porous ceramics*. Dissertations of University of Groningen.

BERRY M.V, HANNAY J.H. 1978. *Topography of Random Surfaces*. Nature, 271: 573.

BHUSHAN B. 1999. *Introduction – Measurement Techniques and Applications. Handbook of Micro/Nanotribology*. Ed. Bharat Bhushan. CRC Press LLC, Boca Raton.

BOJAR Z., KOMOREK Z., DUREJKO T. 1996. *Struktura i właściwości intermetalicznych powłok ochronnych otrzymywanych metodą detonacyjną*. Solidification of Metals and Alloys, 27: 115-119.

BYSTRZYCKI J., VARIN R.A, BOJAR Z. 1996. *Postępy w badaniach stopów na bazie uporządkowanych faz międzymetalicznych z udziałem aluminium*. Inżynieria Materiałowa, 5: 137-149.

CINCA N., GUILEMANY J.M. 2012. *Thermal spraying of transition metal aluminides: An overview*. Intermetallics, 24: 60-72.

CHEN Y., LIANG X., WEI S., LIU Y., XU B. 2009. *Heat treatment induced intermetallic phase transition of arc-sprayed coating prepared by the wires combination of aluminum-cathode and steel-anode*. Applied Surface Science, 255(19): 8299-8304.

CHROSTEK T., RYCHLIK K., BRAMOWICZ M., SENDEROWSKI C. 2018. *Functional and fractal properties of Fe-Al coatings after gas detonation spraying (GDS)*. Archives of Metallurgy and Materials, 63(4): 1991-1997.

HEJWOWSKI T. 2013. *Nowoczesne powłoki nakładane cieplnie odporne na zużycie ścierne i erozyjne*. Monografie, Politechnika Lubelska, Lublin.

JASIONOWSKI R., PRZETAKIEWICZ W., ZASADA D. 2011. *The effect of structure on the cavitational wear of Fe-Al intermetallic phase-based alloys with cubic lattice*. Archives of Foundry Engineering, 11(2): 97-102.

JASIONOWSKI R., BRYLL K., GRABIAN J. 2012. *Badanie właściwości tribologicznych intermetali*. Archives of Foundry Engineering, 12: 87-90.

MAINSAH E., GREENWOOD J.A., CHETWYND D.G. 2001. *Metrology and Properties of Engineering Surfaces*. Kluwer Academic Publishers.

MUŠALEK R., KOVAŘIK O., SKIBA T., HAUŠILD P., KARLIK M., COLMENARES-ANGULO J. 2010. *Fatigue properties of Fe-Al intermetallic coatings prepared by plasma spraying*. Intermetallics, 18: 1415-1418.

NIEWIELKI G., JABŁOŃSKA M. 2007. *Charakterystyka i zastosowanie intermetali z układu Fe-Al*. Inżynieria Materiałowa, 2: 43-47.

SAYLES R.S., THOMAS T.R. 1978. *Surface Topography as a Nonstationary Random Process*. Nature, 271: 431–434.

SCHNEIBEL J.H., RITCHIE R.O., KRUZIC J.J., TORTORELLI P.F. 2005. *Optimization of Mo-Si-B Intermetallic Alloys*. Metallurgical and Materials Transaction A, 36(3): 525-531.

SENDEROWSKI C., ASTACHOV E., BOJAR Z., BORISOV Y. 2011. *Elementarne mechanizmy formowania powłoki intermetalicznej Fe-Al podczas natryskiwania gazodetonacyjnego*. Inżynieria Materiałowa, 4: 719-723.

SENDEROWSKI C. 2015. *Żelazowo-aluminiowe intermetaliczne systemy powłokowe uzyskiwane z naddźwiękowego strumienia metalizacyjnego*. Bel Studio Sp. z o.o., Warszawa.
SZULC T. 2013. *Notatki z historii natryskiwania termicznego*. Przegląd Spawalnictwa, 85(6): 76-83.
XU B., ZHU Z., MA S., ZHANG W., LIU W. 2004. *Sliding wear behavior of Fe-Al and Fe-Al/WC coatings prepared by high velocity arc spraying*. Wear, 257(11): 1089-1095.
YAN D., YANG Y., DONG Y., CHEN X., WANG L., ZHANG J. 2012. *Phase transitions of plasma sprayed FeAl intermetallic coating during corrosion in molten zinc at 640°C*. Intermetallics, 22: 160-165.
ŻÓRAWSKI W. 2010. *Właściwości powłok natryskanych plazmowo i HVOF*. Tribologia, 6: 319-327.

Technical Sciences, 2019, 22(3), 263–270

UNIWERSYTET WARMIŃSKO-MAZURSKI W OLSZTYNIE

Quarterly peer-reviewed scientific journal
ISSN 1505-4675
e-ISSN 2083-4527
TECHNICAL SCIENCES
Homepage: www.uwm.edu.pl/techsci/

doi: 10.31648/ts.4380

VEHICLE NAVIGATION SYSTEMS INVOLVING INERTIAL SENSORS AND ODOMETRY DATA FROM ON-BOARD DIAGNOSTICS IN NON-GPS APPLICATIONS*

***Piotr Prusaczyk*[1], *Leszek Baranowski*[2], *Jarosław Panasiuk*[3]**

[1]ORCID: 0000-0002-1347-1202
Faculty of Mechatronics and Aerospace
Military University of Technology in Warsaw
[2]ORCID: 0000-0002-5239-0659
Faculty of Mechatronics and Aerospace
Military University of Technology in Warsaw
[3]ORCID: 0000-0001-8480-1654
Faculty of Mechatronics and Aerospace
Military University of Technology in Warsaw

Received 8 July 2019, accepted 5 February 2020, available online 7 February 2020.

Keywords: Odometry, Inertial systems, Vehicle Positioning, Land Navigation, On-Board Diagnostic System.

Abstract

This paper explores the applicability of on-board diagnostics data for minimizing inertial navigation errors in vehicles. The results of driving tests were presented and discussed. Knowledge of a vehicle's exact initial position and orientation was crucial in the navigation process. Orientation errors at the beginning of navigation contributed to positioning errors. GPS data were not processed by the algorithm during navigation.

Correspondence: Piotr Prusaczyk, Zespół Mechatroniki, Katedra Mechatroniki, Wydział Mechatroniki i Lotnictwa, Wojskowa Akademia Techniczna, ul. gen. Sylwestra Kaliskiego 2, 00-908 Warszawa 46, e-mail: piotr.prusaczyk@wat.edu.pl.

* Research notes (short communications).

Introduction

Knowledge of a vehicle's position and velocity is essential for many applications, in particular in outdoor vehicles. GPS is widely used for accurate and robust localization. Unfortunately, pure GPS localization can be highly inaccurate in urban environments such as tunnels and urban canyons. In specific situations, the GPS signal can be jammed or turned off. For these reasons, there is a high demand for other navigation techniques (PRUSACZYK et al. 2018a). Inertial navigation systems are theoretically optimal because they do not require external signals to estimate an object's movement. Such systems integrate measurements of rotation and acceleration rate to estimate an object's position. However, accelerometers and gyroscopes do not support accurate positioning during prolonged operation due to data drift (TITTERTON, WESTON 2004). In land navigation, wheel encoders that compute odometry are cost-effective and convenient solutions for determining changes in position, especially in wheeled mobile robots (KACZMAREK, et al. 2017). The data acquired by electronic on-board diagnostic (OBD) systems in vehicles can be used for self-localization (MERRIAUX et al. 2014).

The aim of this study was to propose a navigation method based on inertial and odometry data. The XSens inertial measurement unit (IMU) was used to measure acceleration and rotation speed. Odometry data were provided by the OBD system. The experiment was conducted on the assumption that the vehicle's initial position and orientation are known.

The next section of this paper overviews inertial systems. The following section contains a short introduction to OBD systems. Hardware implementation, including the OBD Reader and the XSens Inertial Measurement Unit, is discussed in the subsequent chapter. The experimental design and research methodology are presented in the Materials and Methods section. The results of the navigation experiment performed in a real-world environment are discussed, and the relevant conclusions are formulated in the last sections.

Inertial Navigation System

Inertial navigation systems (INS) are entirely self-contained in a moving object, and they are not dependent on external radio or optical signals. These systems rely on the inertial properties of navigation sensors that are mounted in moving objects. The system processes data from three-dimensional linear accelerometers and three-dimensional inertial angular rate sensors. The system calculates an object's position and changes in orientation over time (Fig. 1). The information about a vehicle's position and orientation at the beginning of navigation is required to determine the vehicle's position and velocity without the use of external data. In modern INS, sensors are attached to

the vehicle body, which eliminates the mechanical complexity of platform systems. The use of silicon chips has considerably reduced the size and number of system components, which contributed to a reduction in costs. The MEMS gyroscope is non-rotating device that relies on the Coriolis force acting on a vibrating proof mass to calculate inertial angular rotation. The main disadvantages of MEMS gyroscopes include increasing computing complexity and the need to use sensors capable of measuring higher rates of turn (PRUSACZYK et al. 2018a).

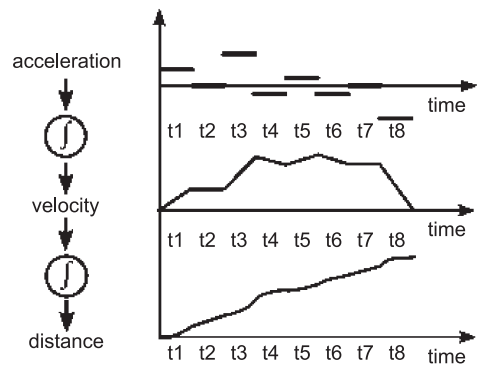

Fig. 1. Integration process

On-Board Diagnostic System

On-Board Diagnostics (OBD) is a term that refers to a computer-based system where an electronic control unit (ECU) collects input data from various sensors to control the actuators and reach the desired performance parameters (Fig. 2).

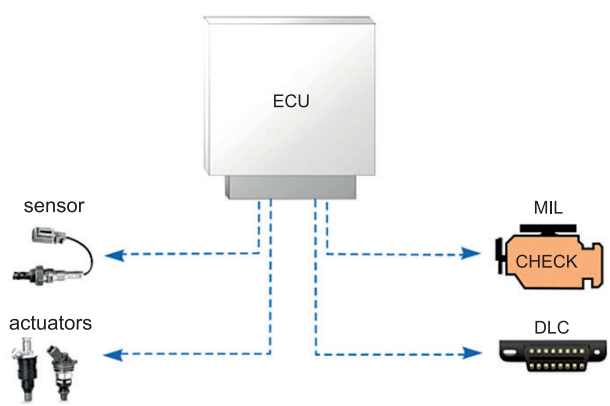

Fig. 2. Diagram of an OBD system

The "Check Engine" light, also known as the Malfunction Indicator Light (MIL), is an early warning of a vehicle malfunction. A modern vehicle can process hundreds of parameters accessed via a Data Link Connector (DLC) which interfaces a scan tool with a vehicle's control module.

The first version of the OBD system standard was introduced in 1985. The OBD system was implemented to improve in-use emissions compliance by alerting the vehicle operator when a malfunction exist, and to aid automobile repair technicians in identifying and repairing malfunctioning circuits in the emissions control system (GAURI et al. 2017).

Materials and Methods

OBD Reader

In the present experiment, the OBD Reader was used to gather information from the OBD system. The OBD Reader was designed by the authors to export data frames from a vehicle's subsystems such as the Engine Control Unit (ECU) and the Automatic Brake System (ABS). Data frames are converted and sent to a PC via a USB port (Fig. 3). Data are converted by an 8-bit microprocessor and a K-line interface chip (PRUSACZYK et al. 2018b).

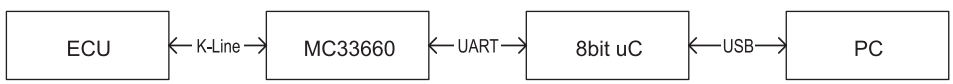

Fig. 3. OBD Reader model

XSens Inertial Measurement Unit

In this experiment, the XSens MTI-G30 Inertial Measurement Unit (IMU) was used to measure linear accelerations and rotational speeds acting on the object (Fig. 4).

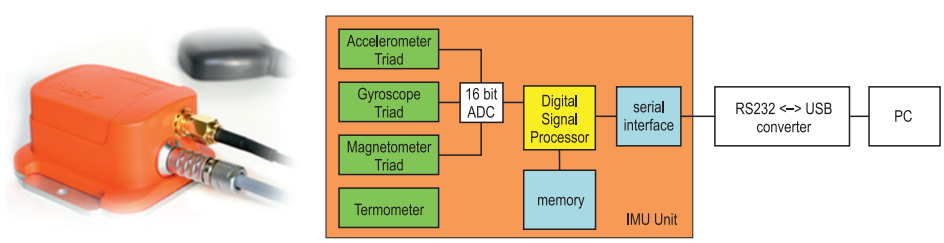

Fig. 4. XSens IMU (*a*), diagram of the test stand (*b*)
Source: based on XSens, www.xsens.com.

Hardware Integration

The XSens IMU and the OBD Reader communicated via a USB interface (Fig. 5). Both devices were controlled by a PC (PRUSACZYK et al. 2018b).

Fig. 5. Hardware connection diagram

Experimental Design

The performance of the inertial navigation system was analysed in an experiment conducted in a real-world environment. The test route was developed based on digital map data and the below parameters:

– Test distance – around 2,000 meters,
– Several reorientation points.

The experimental data were acquired with dedicated communication software and processed in the MATLAB environment. GPS data were collected as real position data during the experiment for the purpose of verification and comparison.

Results

The experiment was performed in city traffic. The following characteristics of the generated route were extracted (Fig. 6):

– Final reorientation of the vehicle – above 360°,
– Several reorientation points (multiple turns),
– Test distance – 2,030 meters.

The vehicle's orientation relative to three axes is presented in Figure 7. The right-most diagram shows the heading of the vehicle. Several changes in the vehicle's heading can be observed when turning at a junction.

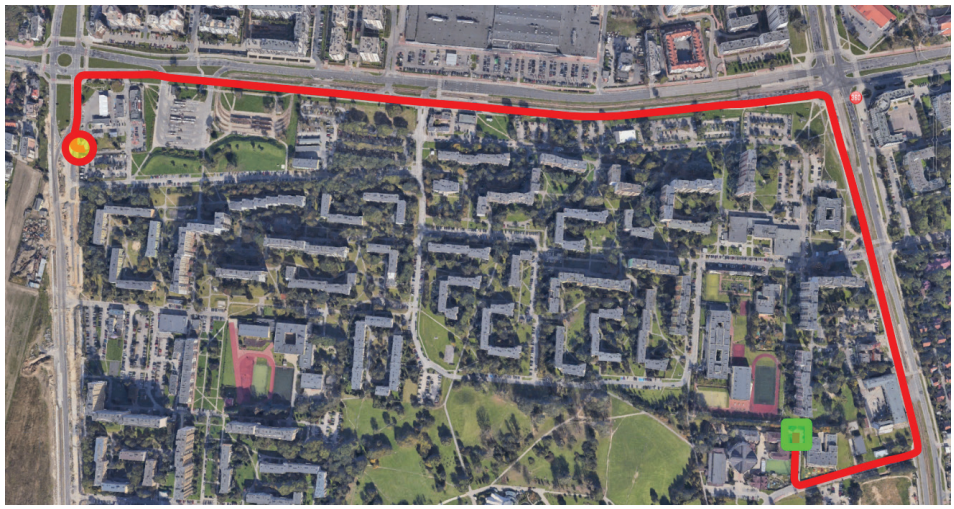

Fig. 6. Experimental path

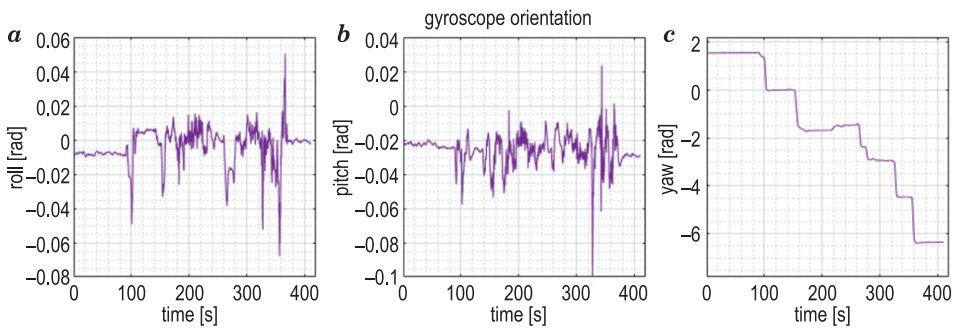

Fig. 7. Recorded gyroscope orientation around x axis (a), y axis (b) and z axis (c)

The three sources of velocity data are presented in Figure 8. The first is the inertial navigation system assisted by Zero Update Velocity (ZUPT) which detects stationary states for resetting the inertial sensor. The second source is the OBD system, and the third source is the reference speed from a calibrated GPS sensor.

The velocity measurements acquired by the assisted inertial navigation method contained errors relative to the data obtained by the OBD-assisted odometry method. The iterations of inertial velocity data could be responsible for significant differences in estimates of the vehicle's position.

The path shape estimated by the inertial navigation system aided by OBD odometry is similar to that estimated by GPS (Fig. 9), with some differences (Fig. 10) caused by hardware errors.

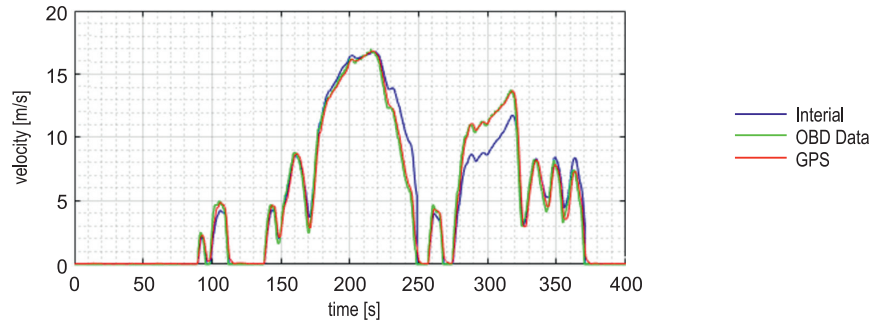

Fig. 8. Registered velocity

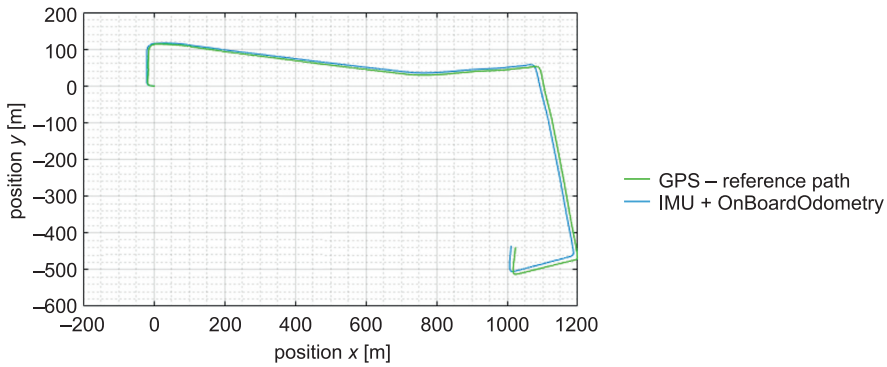

Fig. 9. Obtained trajectory

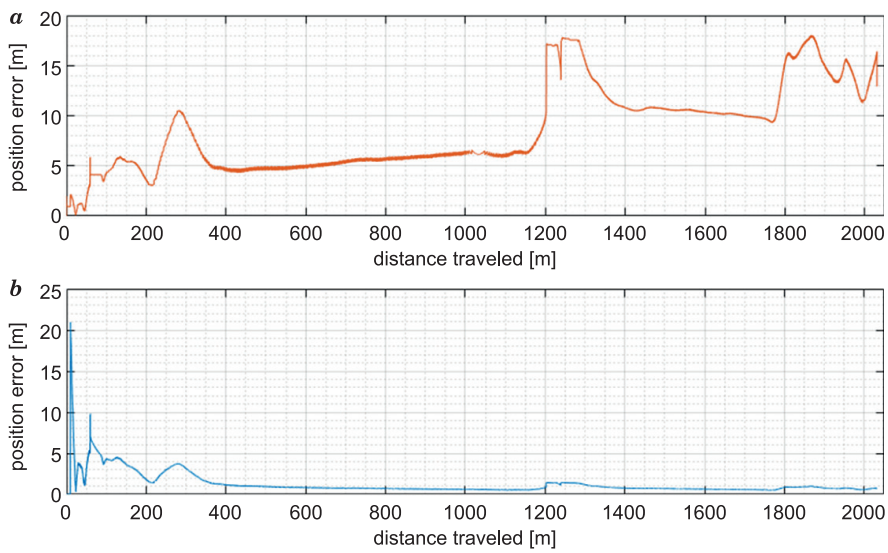

Fig. 10. Position error in meters (*a*) and percentage of travelled distance (*b*)

Fewer navigation errors were generated than in the standalone inertial navigation system. During the experiment, the position error remained stable over time. Position errors as a function of the travelled distance are presented in Figure 10.

Conclusions

A practical application of non-GPS navigation based on inertial sensors and odometry data from a vehicle's On-Board Diagnostic system was presented in this article. Unlike in pure inertial navigation systems, the number of errors in odometry-assisted systems increases only with the travelled distance. Position errors remained stable during the experiment, but the tested solution cannot be applied in long-term navigation scenarios. Additional sources of data are needed to minimize the increase in the number of position errors.

An algorithm for determining a vehicle's initial position without a GPS signal will be implemented in future research.

References

GAURI M., PARCHANDEKAR S.K., TAHIR M. 2017. *Implementation and Validation of K Line (ISO 9141) Protocol for Diagnostic Application.* International Research Journal of Engineering and Technology, 4(7): 713-708.

KACZMAREK W., PANASIUK J., PRUSACZYK P., BESSEGHIEUR K. 2017. *Formation control of mobile robots under ROS.* Proceedings of the 23rd International Conference – Engineering Mechanics, p. 138–141.

MERRIAUX P., DUPUIS Y., VASSEUR P., SAVATIER X. 2014. *Wheel odometry-based car localization and tracking on vectorial map.* IEEE, 14: 1890-1891.

PRUSACZYK P., PANASIUK J., BARANOWSKI L. 2018a. *GPS-free navigation based on using inertial and odometry, data fusion and map matching algorithm.* AIP Conference Proceedings 14th International Conference Mechatronic Systems and Materials, 2029(20062).

PRUSACZYK P., PANASIUK J., BARANOWSKI L. 2018b. *Opracowanie interfejsu wymiany danych między użytkownikiem a samochodem.* Problemy Mechatroniki. Uzbrojenie, Lotnictwo, Inżynieria Bezpieczeństwa, 9(2): 147-156.

TITTERTON D., WESTON J. 2004. *Strapdown Inertial Navigation Technology*. 2nd Edition. The Institution of Engineering and Technology, Michael Faraday House, Six Hills Way, Stevenage, Herts.

Xsens MTi-G. 2019. http://www.xsens.com.

Technical Sciences, 2019, 22(3), 271–280

UNIWERSYTET WARMIŃSKO-MAZURSKI W OLSZTYNIE

Quarterly peer-reviewed scientific journal
ISSN 1505-4675
e-ISSN 2083-4527
TECHNICAL SCIENCES
Homepage: www.uwm.edu.pl/techsci/

doi: 10.31648/ts.5293

THE USE OF A BEAD MILL FOR THE PRODUCTION OF AGROCHEMICAL SUSPENSIONS

***Katarzyna Szwedziak*[1], *Żaneta Grzywacz*[2], *Sławomir Tomaszewski*[3]**

[1]ORCID: 0000-0003-1104-5143
Department of Biosystems Engineering
Opole University of Technology, Opole
[2]ORCID: 0000-0001-6278-6924
Department of Biosystems Engineering
Opole University of Technology, Opole
[3]Pestila Sp. z o.o., Studzianki

Received 7 October 2019, accepted 18 February 2020, available online 19 February 2020.

K e y w o r d s: suspension, bead mill, plant protection products, formulation, fungicides, liquid chromatography.

A b s t r a c t

Plant protection products represent one of the most innovative branches of the agrochemical industry which requires considerable financial investment to adequately meet agricultural needs. The optimal agrochemicals should enable farmers to maximize yields, and their components should remain active over long periods of time regardless of weather conditions.

This article describes an innovative technology for the production of agrochemical suspensions in a bead mill. The suspension acts as a carrier of active ingredients. The parameters of the bead mill were presented, and the resulting suspensions were used in the production of fungicides.

The parameters of the substrates used in the production of agrochemicals have to comply with legal regulations. The present experiment involved liquid chromatography, and it was conducted in accordance with good practice, in line with CIPAC guidelines.

Correspondence: Żaneta Grzywacz, Katedra Inżynierii Biosystemów, Politechnika Opolska, ul. S. Mikołajczyka 5, 45-271 Opole, phone: 48 77 449 8880, e-mail: z.grzywacz@po.opole.pl

Introduction

The main goal of plant protection products is to protect cultivated plant species against risk factors. Despite the fact that plant protection products often raise controversy, their application cannot be drastically reduced or discontinued because such measures would lead to a sudden decrease in the yield and quality of crops. High start-up costs and high product quality requirements are one of the main barriers to entering the agrochemicals market. The production of high-quality compounds and substrates with the required physical and chemical properties plays a very important role, especially in view of the fact that manufacturers often store chemical substances for further production. These substances are exposed to various external factors during storage (SZWEDZIAK et al. 2019).

Despite the fact that the modern market caters to the manufacturers' needs by offering dedicated production technologies and machines, these solutions are expensive and they do not always fulfil the consumers' expectations regarding the quality of the offered products. Therefore, in an attempt to increase their market share, local producers search for new production technologies that guarantee the high quality of plant protection products.

The quality of plant protection products is evaluated by analysing their physical and chemical parameters, including suspension stability, emulsion stability, wetting time, sieve residue, specific gravity, solution stability, and degree of solubility. The products are subjected to quality control in line with EU requirements to determine whether the quality parameters of the products present on the market are consistent with the parameters declared by the manufacturer in the registration process.

Therefore, an analysis of the problems faced by the manufacturers of plant protection products has prompted the authors to search for a generally available, easy-to-use and innovative technology that would facilitate the production of new agrochemicals that meet the expectations of both consumers and producers. Effective agrochemical production systems play an important role in industry and agriculture, and their continued development merits new research.

In the present experiment, a bead mill was used to guarantee the high quality of suspensions for the production of plant protection products. The proposed technology relies on a bead mill instead of a ball meal to obtain suspensions that act as carriers of active ingredients in plant protection products. The effectiveness of the new suspension production technology has not been investigated to date. The system has never been tested in an industrial setting in Poland. Agrochemical factories rely on dispersing and homogenizing machines to produce suspensions with the appropriate parameters for the production of plant protection products. Different types of mills cannot be compared directly, and their performance is difficult to scale. Parameters such as the efficiency and

energy consumption of milling systems are critical for assessing the machines' suitability for specific applications (NAPIER-MUNN 1997). Grinding is a highly energy-consuming process, and it has been researched extensively in scientific and industrial literature around the world (GAWENDA 2009, 2010).

Fine grinding drum mills are the most widely used devices in the agrochemical industry. The material inside drum mills is ground by impact and abrasion. Industrial mills are classified into ball or rod depending on the type of grinding elements (grinding media) (TUMIDAJSKI et al. 2010). In traditional ball or rod drum mills, grinding media are set into motion by the rotation of the mill drum (cylindrical working chamber filled with grinding media) (SIDOR 2015).

The aim of this study was to develop a new technology for the production of suspensions for plant protection products in a bead mill, to obtain raw materials of the highest possible quality for the production of those agrochemicals, and to determine the content of the active ingredient in the obtained formulation.

Materials and Methods

The experiment involved a bead mill operating in a continuous system in a machine hall and a laboratory mill in a chemical laboratory (Figs. 1, 2).

The bead mill had the following parameters:

– Zirconia beads 0.8-1.0 mm, 150 kg;
– Chemical composition: ZrO_2 – 83%, CeO_2 – 17%;
– Density: 6.20 gm/cm^3 (+/-0.05);
– Bulk density: 3.75-4.05 kg/l;
– Hardness on the Mohs scale: 9.

The structure of the bead mill is shown in Figure 3. The test stand comprising a laboratory bead mill is presented in Figures 1 and 2.

Fig. 1. Test stand – laboratory bead mill

Fig. 2. Test stand – bead mill in the machine hall

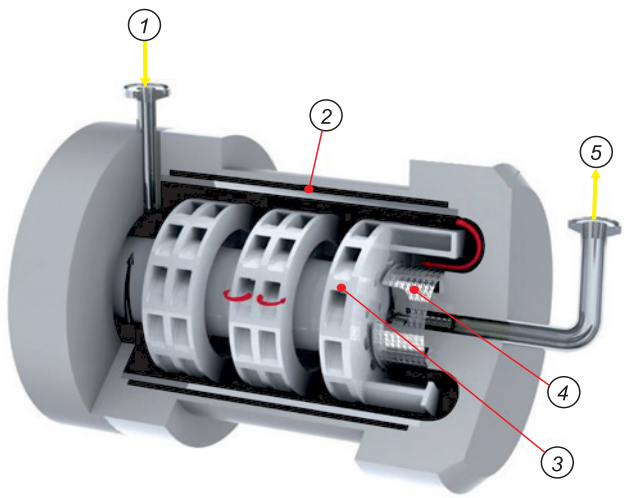

Fig. 3. Diagram of a bead mill: *1* – cooling milling container with easy-to-replace grinding cylinder made of hardened or stainless steel, silicon carbide and zirconia, *2* – agitator disks made of stainless steel, hardened steel, zirconia, tungsten carbide, polyurethane and polyamide, *3* – product inlet, *4* – dynamic gap separator, *5* – product outlet, *6* – accelerators made of hardened chromium alloy, polyethylene oxide or zirconia

The tested compound was metazachlor which is an active ingredient in commercially active pesticides. The Metazachlor 500 S.C. pesticide was used in the experiment.

The formulations containing metazachlor as the active ingredient were subjected to 25 series of tests that were carried out in triplicate. The tested products were subjected to qualitative analyses to determine the content of the active ingredient (metazachlor) in g/l, density at 20°C g/l, and pH. All tests were

conducted in accordance with good laboratory practices based on the guidelines of the Collaborative International Pesticides Analytical Council (CIPAC). The methods developed in the industrial sector are rigorously tested in laboratories around the world. If approved, they are published in CIPAC Handbooks (refer to "CIPAC Methods" and "CIPAC Publication"). In this study, the content of the active (ingredient in the tested products was determined by liquid chromatography (IA/HPLC/10).

The content of the active ingredient was determined by preparing standard solutions of this compound and solutions of the tested samples. The eluent was 1% aqueous solution of H_3PO_4 : acetonitrile (50:50) which was used as solvent. The tests were carried out in the Agilent Technologies 1260 Infinity liquid chromatograph.

The content of the active ingredient in the tested products was calculated using the following formula:

$$c = \mathrm{AT}/\mathrm{AS} \cdot \mathrm{MS}/\mathrm{MT} \cdot P \ [\%] \tag{1}$$

where:

c – metazachlor content of the tested products [%],
AT – surface area of metazachlor in the chromatogram of the tested solution,
AS – surface area of metazachlor in the chromatogram of the tested solution,
MS – weighed amount of the standard [mg],
P – standard purity [%].

pH was measured in 1% suspension of the product and directly in the product at 20°C by the potentiometric method (*MT 75.3 Determination of pH values* 2000, p. 131). Relative density was determined with the DMN 4100 M density meter at ambient temperature (*Test No. 109…* 2012, p. 2) All tests were carried out in accordance with the Regulation of the Minister of Health of 22 May 2013 on Good Laboratory Practice and the performance of laboratory analyses in compliance with the principles of Good Laboratory Practice and the provisions of Directive 2004/9/EC of 11 February 2004 amending Council Directive 87/18/EEC of 18 December 1986 (Official Journal of the European Union).

Results and Discussion

The results of the experiment were used to determine the content of the active ingredient, density and pH of the obtained formulation (Figs. 4-6). The results are presented in Table 1 as the means of triplicate measurements.

The results of the analysis indicate that Metazachlor 500 S.C is characterized by a stable content of the active ingredient (metazachlor) as well as stable pH and density. The formulation produced in the bead mill contained 509.1 g/l of the active ingredient on average. It had a pH of 6.7 and density of 1.13 g/ml.

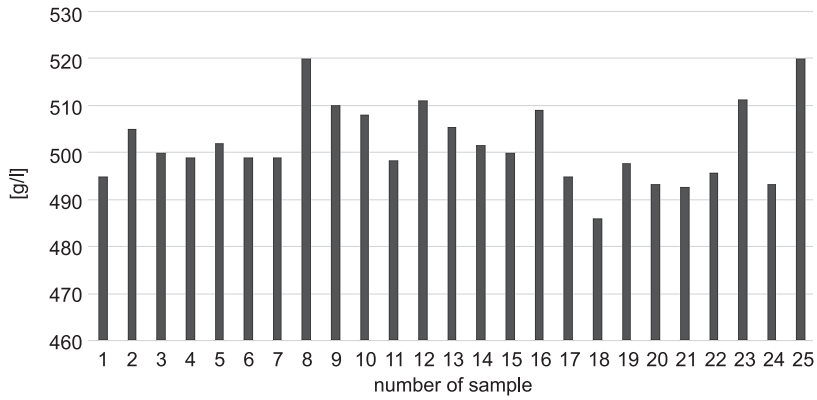

Fig. 4. The content of the active ingredient in individual samples of Metazachlor 500 S.C [g/l]

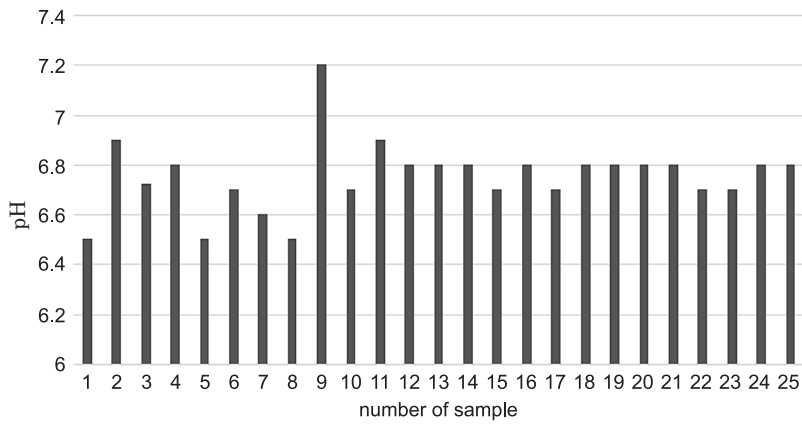

Fig. 5. pH in individual samples of the tested pesticide containing metazachlor as the active ingredient

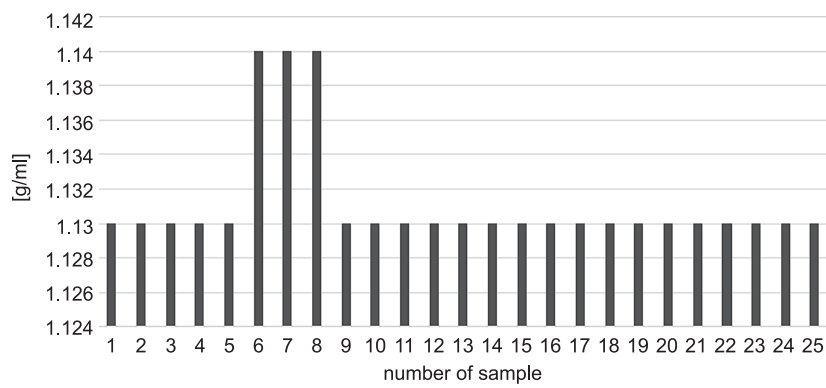

Fig. 6. Density [g/ml] of individual samples of the tested pesticide containing metazachlor as the active ingredient

Table 1

Results of the analysis of the tested product containing metazachlor as the active ingredient

No. of sample	Content of the active ingredient [g/l]	pH	Density [g/ml]
1	495	6.5	1.13
2	505	6.9	1.13
3	500	6.72	1.13
4	499	6.8	1.13
5	502	6.5	1.13
6	499	6.7	1.14
7	499	6.6	1.14
8	520	6.5	1.14
9	510.1	7.2	1.13
10	508	6.7	1.13
11	498.4	6.9	1.13
12	511.1	6.8	1.13
13	505.4	6.8	1.13
14	501.6	6.8	1.13
15	500	6.7	1.13
16	509	6.8	1.13
17	495	6.7	1.13
18	486.1	6.8	1.13
19	497.8	6.8	1.13
20	493.2	6.8	1.13
21	492.6	6.8	1.13
22	495.8	6.7	1.13
23	511.3	6.7	1.13
24	493.2	6.8	1.13
25	520	6.8	1.13
Standard deviation	± 8.38	± 0.14	± 0.00
Variance	70.270	0,021	0.00

The obtained descriptive statistics are presented in Tables 2 and 3. The normality of distribution was checked with the Shapiro-Wilk test for the content of the active ingredient:

$$\text{Maksymus 040 S.C (Shapiro-Wilk test } W=0.877,\ n=24,\ p=0.007)$$

and for pH:

$$\text{Maksymus 040 S.C (Shapiro-Wilk test } W=0.717,\ n=24,\ p=0.05).$$

Table 2

Descriptive statistics for the tested product containing the metazachlor active ingredient

Statistical quantity	METAZACHLOR 500SC		
	content of the substance	pH	density
Number of samples	25	25	25
Mean	501.90	6.75	1.130
Median	500.0	6.8	1.129
Minimum	486.1	6.5	1.13
Maximum	520.0	7.2	1.14
Lower quartile	495.8	6.7	1.13
Upper quartile	508.0	6.8	1.13
Variance	70.270	0.021	0.000
Standard deviation	8.38	0.14	0.00

Table 3

Results of a statistical analysis of the tested product containing metazachlor as the active ingredient for individual confidence intervals

Product	pH 95% confidence interval	pH 99% confidence interval	Density [g/ml] 95% confidence interval	Density [g/ml] 99% confidence interval	Content of the active ingredient [g/l] 95% confidence interval	Content of the active ingredient [g/l] 99% confidence interval
METAZACHLOR 500SC	6.69 – 6.81	6.67 – 6.83	1.130 – 1.133	1.129 – 1.133	498.44 – 505.36	497.21 – 506.59

The results obtained in all 25 tests were within the calculated limits. The content of the active ingredient (70.270 g/l) was the only parameter characterized by a greater scatter of values, which resulted in higher variance. Selected quality parameters of Metazachlor 500 S.C. had been previously analysed in our earlier study which revealed that the content of the active ingredient, pH and density were within the accepted standards, whereas the average metazachlor content varied across products from different batches (SZWEDZIAK et al. 2019).

The calculated confidence intervals indicate that despite higher variance, the content of the active ingredient was within the acceptable limits (Tab. 2). These results suggest that a bead mill is a reasonably efficient solution for manufacturing agrochemical suspensions.

Conclusions

The results of the present study indicate that the tested formulations of plant protection products containing metazachlor as the active ingredient, produced in a bead mill, fulfil the required quality standards. The recommended standards for the manufacture of plant protection products were not exceeded in the formulation produced in a bead mill. This observation was confirmed in an analysis of variance.

Based on the presented results, the following conclusions were drawn:

1. The use of a bead mill filled with zirconia beads (0.8-1.0 mm in size, density – 6.20 gm/cm^3) enabled the production of agrochemicals containing metazachlor as the active ingredient whose parameters were within the acceptable limits. The quality of the manufactured formulation was consistent with the relevant standards.

2. The use of a bead mill ensures that the formulations of plant protection products containing metazachlor as the active ingredient will conform to the applicable standards at a 99% confidence level. These results were confirmed statistically.

3. The use of a bead mill guarantees that metazachlor-based formulations will conform to the required standards in the production of fungicides where metazachlor is the active ingredient.

References

Directive 2004/9/EC of 11 February. 2004. Amending Council Directive 87/18/EEC, Official Journal of the European Union.

GAWENDA T. 2009. *Main aspects of grinding hard mineral raw materials in high-pressure roller presses*. Mining and Geoengineering, 33(4).

GAWENDA T. 2010. *Problems with the selection of crushing machines in mineral aggregate installations*. Mining and Geoengineering, 34(4).

IA/HPLC/10. Laboratory Procedure.

MT 75.3 Determination of pH values. 2000. CIPAC Handbook, J: 131.

NAPIER-MUNN T.J., MORRELL S., MORRISON R.D., KOJOVIC T. 1997. *Mineral comminution circuits – Their operation and optimization*. JKMRC monograph series in mining and mineral processing. Hall & Jones Pty Ltd., Brisbane, p. 413.

SIDOR J., FOSZCZ D., TOMACH P., KRAWCZYKOWSKI D. 2015. *High-energy mills for grinding ores and mineral resources*. CUPRUM, 2: 71-85.

SZWEDZIAK K., GRZYWACZ Ż., BIŁOS Ł., TOMASZEWSKI S. 2019. *Physicochemical properties of containing azoxystrobin AZS–GEN 250 SC after 2 years of storage*. Chemical Industry, 98(3): 372-376, doi: 10.15199/62.2019.3.4.

SZWEDZIAK K., TUKIENDORF M., GRZYWACZ Ż., TOMASZEWSKI S., WOJTKIEWICZ W. 2019. *Physicochemical properties of a commercial herbicidal product containing metazachlor as an active substance*. Chemical Industry, 98(7): 1113-1117, doi: 10.15199/62.2019.7.16.

Test No. 109 Density of Liquids and Solids. 2012. OECD, p. 2.
The Regulation of the Minister of Healt of 22 May 2013 on Good Laboratory Practice and Performance of Studies in Compilance with the Principces of Good Laboratory Practice.
TUMIDAJSKI T., KASIŃSKA-PILUT E., GAWENDA T., NAZIEMIEC Z., PILUT R. 2010. *Research on energy consumption of the grinding process and susceptibility to grinding of lithological components of Polish copper ores.* Economy of Mineral Raw Materials, 26(1): 61-72.

Guide for Autors

Introduction

Technical Sciences is a peer-reviewed research Journal published in English by thePublishing House of the University of Warmia and Mazury in Olsztyn (Poland). Journal is published continually since 1998. Until 2010 Journal was published as a yearbook, in 2011 and 2012 it was published semiyearly. From 2013, the Journal is published quarterly in the spring, summer, fall, and winter.

The Journal covers basic and applied researches in the field of engineering and the physical sciences that represent advances in understanding or modeling of the performance of technical and/or biological systems. The Journal covers most branches of engineering science including biosystems engineering, civil engineering, environmental engineering, food engineering, geodesy and cartography, information technology, mechanical engineering, materials science, production engineering etc.

Papers may report the results of experiments, theoretical analyses, design of machines and mechanization systems, processes or processing methods, new materials, new measurements methods or new ideas in information technology.

The submitted manuscripts should have clear science content in methodology, results and discussion. Appropriate scientific and statistically sound experimental designs must be included in methodology and statistics must be employed in analyzing data to discuss the impact of test variables. Moreover there should be clear evidence provided on how the given results advance the area of engineering science. Mere confirmation of existing published data is not acceptable. Manuscripts should present results of completed works.

There are three types of papers: a) research papers (full length articles); b) short communications; c) review papers.

The Journal is published in the printed and electronic version. The electronic version is published on the website ahead of printed version of Technical Sciences.

Technical Sciences does not charge submission or page fees.

Types of paper

The following articles are accepted for publication:

Reviews

Reviews should present a focused aspect on a topic of current interest in the area of biosystems engineering, civil engineering, environmental engineering, food engineering, geodesy and cartography, information technology, mechanical engineering, materials science, production engineering etc. They should include all major findings and bring together reports from a number of sources. These critical reviews should draw out comparisons and conflicts between work, and provide an overview of the 'state of the art'. They should give objective assessments of the topic by citing relevant published work, and not merely present the opinions of individual authors or summarize only work carried out by the authors or by those with whom the authors agree. Undue speculations should also be avoided. Reviews generally should not exceed 6,000 words.

Research Papers

Research Papers are reports of complete, scientifically sound, original research which contributes new knowledge to its field. Papers should not exceed 5,000 words, including figures and tables.

Short Communications

Short Communications are research papers constituting a concise description of a limited investigation. They should be completely documented, both by reference list, and description of the experimental procedures. Short Communications should not occupy more than 2,000 words, including figures and tables.

Letters to the Editor

Letters to the Editor should concern with issues raised by articles recently published in scientific journals or by recent developments in the engineering area.

Contact details for submission

The paper should be sent to the Editorial Office, as a Microsoft Word file, by e-mail: techsci@uwm.edu.pl

Referees

Author/authors should suggest, the names, addresses and e-mail addresses of at least three potential referees. The editor retains the sole right to decide whether or not the suggested reviewers are used.

Submission declaration

After final acceptance of the manuscript, the corresponding author should send to the Editorial Office the author's declaration. Submission of an article implies that the work has not been published previously (except in the form of an abstract or as part of a published lecture or academic thesis or as an electronic preprint), that it is not under consideration for publication elsewhere, that publication is approved by all authors and tacitly or explicitly by the responsible authorities where the work was carried out, and that, if accepted, it will not be published elsewhere in the same form, in English or in any other language.

To prevent cases of ghostwriting and guest authorship, the author/authors of manuscripts is/are obliged to: (i) disclose the input of each author to the text (specifying their affiliations and contributions, i.e. who is the author of the concept, assumptions, methods, protocol, etc. used during the preparation of the text); (ii) disclose information about the funding sources for the article, the contribution of research institutions, associations and other entities.

Language

Authors should prepare the full manuscript i.e. title, abstract and the main text in English (American or British usage is accepted). Polish version of the manuscript is not required.

The file type

Text should be prepared in a word processor and saved in doc or docx file (MS Office).

Article structure

Suggested structure of the manuscript is as follows:

Title
Authors and affiliations
Corresponding author
Abstract
Keywords
Introduction
Material and Methods
Results and Discussion
Conclusions

Acknowledgements (optional)
References
Tables
Figures

Subdivision – numbered sections

Text should be organized into clearly defined and numbered sections and subsections (optionally). Sections and subsections should be numbered as 1. 2. 3. then 1.1 1.2 1.3 (then 1.1.1, 1.1.2, …). The abstract should not be included in numbering section. A brief heading may be given to any subsection. Each heading should appear on its own separate line. A single line should separate paragraphs. Indentation should be used in each paragraph.

Font guidelines are as follows:

– Title: 14 pt. Times New Roman, bold, centered, with caps
– Author names and affiliations:12 pt. Times New Roman, bold, centered, italic, two blank line above
– Abstract: 10 pt. Times New Roman, full justified, one and a half space. Abstract should begin with the word Abstract immediately following the title block with one blank line in between. The word Abstract: 10 pt. Times New Roman, centered, indentation should be used
– Section Headings: Not numbered, 12 pt. Times New Roman, bold, centered; one blank line above
– Section Sub-headings: Numbered, 12 pt. Times New Roman, bold, italic, centered; one blank line above
– Regular text: 12 pt. Times New Roman, one and a half space,full justified, indentation should be used in each paragraph

Title page information

The following information should be placed at the first page:

Title

Concise and informative. If possible, authors should not use abbreviations and formulae.

Authors and affiliations

Author/authors' names should be presented below the title. The authors' affiliation addresses (department or college; university or company; city, state and zip code, country) should be placed below the names. Authors with the same affiliation must be grouped together on the same line with affiliation information following in a single block. Authors should indicate all affiliations with a lower-case superscript letter immediately after the author's name and in front of the appropriate address.

Corresponding author

It should be clearly indicated who will handle correspondence at all stages of refereeing and publication, also post-publication process. The e-mail address should be provided (footer, first page). Contact details must be kept up to date by the corresponding author.

Abstract

The abstract should have up to 100-150 words in length. A concise abstract is required. The abstract should state briefly the aim of the research, the principal results and major conclusions. Abstract must be able to stand alone. Only abbreviations firmly established in the field may be eligible. Non-standard or uncommon abbreviations should be avoided, but if essential they must be defined at their first mention in the abstract itself.

Keywords

Immediately after the abstract, author/authors should provide a maximum of 6 keywords avoiding general, plural terms and multiple concepts (avoid, for example, 'and', 'of'). Author/authors should be sparing with abbreviations: only abbreviations firmly established in the field may be eligible.

Abbreviations

Author/authors should define abbreviations that are not standard in this field. Abbreviations must be defined at their first mention there. Author/authors should ensure consistency of abbreviations throughout the article.

Units

All units used in the paper should be consistent with the SI system of measurement. If other units are mentioned, author/authors should give their equivalent in SI.

Introduction

Literature sources should be appropriately selected and cited. A literature review should discuss published information in a particular subject area. Introduction should identify, describe and analyze related research that has already been done and summarize the state of art in the topic area. Author/authors should state clearly the objectives of the work and provide an adequate background.

Material and Methods

Author/authors should provide sufficient details to allow the work to be reproduced by other researchers. Methods already published should be indicated by a reference. A theory should extend, not repeat, the background to the article already dealt within the Introduction and lay the foundation for further work. Calculations should represent a practical development from a theoretical basis.

Results and Discussion

Results should be clear and concise. Discussion should explore the significance of the results of the work, not repeat them. A combined Results and Discussion section is often appropriate.

Conclusions

The main conclusions of the study may be presented in a Conclusions section, which may stand alone or form a subsection of a Results and Discussion section.

Acknowledgements

Author/authors should include acknowledgements in a separate section at the end of the manuscript before the references. Author/authors should not include them on the title page, as a footnote to the title or otherwise. Individuals who provided help during the research study should be listed in this section.

Artwork

General points

– Make sure you use uniform lettering and sizing of your original artwork
– Embed the used fonts if the application provides that option
– Aim to use the following fonts in your illustrations: Arial, Courier, Times New Roman, Symbol
– Number equations, tables and figures according to their sequence in the text
– Size the illustrations close to the desired dimensions of the printed version

Formats

If your electronic artwork is created in a Microsoft Office application (Word, PowerPoint, Excel) then please supply 'as is' in the native document format

Regardless of the application used other than Microsoft Office, when your electronic artwork is finalized, please 'Save as' or convert the images to one of the following formats (note the resolution requirements given below):

EPS (or PDF): Vector drawings, embed all used fonts

JPEG: Color or grayscale photographs (halftones), keep to a minimum of 300 dpi

JPEG: Bitmapped (pure black & white pixels) line drawings, keep to a minimum of 1000 dpi or combinations bitmapped line/half-tone (color or grayscale), keep to a minimum of 500 dpi

Please do not:

– Supply files that are optimized for screen use (e.g., GIF, BMP, PICT, WPG); these typically have a low number of pixels and limited set of colors
– Supply files that are too low in resolution
– Submit graphics that are disproportionately large for the content

Color artwork

Author/authors should make sure that artwork files are in an acceptable format (JPEG, EPS PDF, or MS Office files) and with the correct resolution. If, together with manuscript, author/authors submit color figures then Technical Sciences will ensure that these figures will appear in color on the web as well as in the printed version at no additional charge.

Tables, figures, and equations

Tables, figures, and equations/formulae should be identified and numbered consecutively in accordance with their appearance in the text.

Equations/mathematical and physical formulae should be presented in the main text, while tables and figures should be presented at the end of file (after References section). Mathematical and physical formulae should be presented in the MS Word formula editor.

All types of figures can be black/white or color. Author/authors should ensure that each figure is numbered and has a caption. A caption should be placed below the figure. Figure must be able to stand alone (explanation of all symbols and abbreviations used in figure is required). Units must be always included. It is noted that figure and table numbering should be independent.

Tables should be numbered consecutively in accordance with their appearance in the text. Table caption should be placed above the table. Footnotes to tables should be placed below the table body and indicated with superscript lowercase letters. Vertical rules should be avoided. Author/authors should ensure that the data presented in tables do not duplicate results described in figures, diagrams, schemes, etc. Table must be able to stand alone (explanation of all symbols and abbreviations used in table is required). Units must be always included. As above, figure and table numbering should be independent.

References

References: All publications cited in the text should be presented in a list of references following the text of the manuscript. The manuscript should be carefully checked to ensure that the spelling of authors' names and dates of publications are exactly the same in the text as in the reference list. Authors should ensure that each reference cited in the text is also present in the reference list (and vice versa).

Citations may be made directly (or parenthetically). All citations in the text should refer to:

1. Single author

The author's name (without initials, with caps, unless there is ambiguity) and the year of publication should appear in the text

2. Two authors

Both authors' names (without initials, with caps) and the year of publication should appear in the text

3. Three or more authors

First author's name followed by et al. and the year of publication should appear in the text

Groups of references should be listed first alphabetically, then chronologically.

Examples:

"... have been reported recently (ALLAN, 1996a, 1996b, 1999; ALLAN and JONES, 1995). KRAMER et al. (2000) have recently shown..."

The list of references should be arranged alphabetically by authors' names, then further sorted chronologically if necessary. More than once reference from the same author(s) in the same year must be identified by the letters "a", "b", "c" etc., placed after the year of publication.

References should be given in the following form:

KUMBHAR B.K., AGARVAL R.S., DAS K. 1981. Thermal properties of fresh and frozen fish. International Journal of Refrigeration, 4(3), 143–146.

MACHADO M.F., OLIVEIRA F.A.R., GEKAS V. 1997. Modelling water uptake and soluble solids losses by puffed breakfast cereal immersed in water or milk. In Proceedings of the Seventh International Congress on Engineering and Food, Brighton, UK.

NETER J., KUTNER M.H., NACHTSCHEIM C.J., WASSERMAN W. 1966. Applied linear statistical models (4th ed., pp. 1289–1293). Irwin, Chicago.

THOMSON F.M. 1984. Storage of particulate solids. In M. E. Fayed, L. Otten (Eds.), Handbook of Powder Science and Technology (pp. 365–463). Van Nostrand Reinhold, New York.

Citation of a reference as 'in press' implies that the item has been accepted for publication.

Note that the full names of Journals should appear in reference list.

Submission checklist

The following list will be useful during the final checking of an article prior to the submission. Before sending the manuscript to the Journal for review, author/authors should ensure that the following items are present:

– Text is prepared with a word processor and saved in DOC or DOCX file (MS Office). One author has been designated as the corresponding author with contact details: e-mail address
– Manuscript has been 'spell-checked' and 'grammar-checked'
– References are in the correct format for this Journal
– All references mentioned in the Reference list are cited in the text, and vice versa
– Author/authors does/do not supply files that are too low in resolution
– Author/authors does/do not submit graphics that are disproportionately large for the content